

# Detecting pathogenic bacteria in blood with combined acoustic bioprinting, Raman spectroscopy, and machine learning

Fareeha Safir<sup>1\*</sup>, Nhat Vu<sup>2</sup>, Loza F. Tadesse<sup>3</sup>, Kamyar Firouzi<sup>4</sup>, Niaz Banaei<sup>5,6,7</sup>, Stefanie S. Jeffrey<sup>8</sup>, Amr. A. E. Saleh<sup>9,10\*</sup>, Butrus (Pierre) Khuri-Yakub<sup>4,11</sup> and Jennifer A. Dionne<sup>10,12\*</sup>

<sup>1\*</sup>Department of Mechanical Engineering, Stanford University, Stanford, 94305, CA, United States.

<sup>2</sup>Pumpkinseed Technologies, Inc., Palo Alto, 94306, CA, United States.

<sup>3</sup>Department of Bioengineering, Stanford University School of Medicine and School of Engineering, Stanford, 94305, CA, United States.

Present Address: Department of Electrical Engineering and Computer Science, University of California, Berkeley, Berkeley, 94720, CA, United States.

<sup>4</sup>E. L. Ginzton Laboratory, Stanford University, Stanford, 94305, CA, United States.

<sup>5</sup>Department of Pathology, Stanford University School of Medicine, Stanford, 94305, CA, United States.

<sup>6</sup>Clinical Microbiology Laboratory, Stanford Health Care, Palo Alto, 94304, CA, United States.

<sup>7</sup>Department of Infectious Diseases and Geographic Medicine, Stanford University School of Medicine, Stanford, 94305, CA, United States.

<sup>8</sup>Department of Surgery, Stanford University School of Medicine, Stanford, 94305, CA, United States.

<sup>9</sup>Department of Engineering Mathematics and Physics, Cairo University, Cairo, 12613, Egypt.

<sup>10</sup>Department of Materials Science and Engineering, Stanford University, Stanford, 94305, CA, United States.

<sup>11</sup>Department of Electrical Engineering, Stanford University, Stanford, 94305, CA, United States.

<sup>12</sup>Department of Radiology, Molecular Imaging Program at Stanford (MIPS), Stanford University School of Medicine, Stanford, 94035, CA, United States.

\*To whom correspondence should be addressed; E-mail: [fsafir@stanford.edu](mailto:fsafir@stanford.edu); [aessawi@eng.cu.edu.eg](mailto:aessawi@eng.cu.edu.eg); [jdionne@stanford.edu](mailto:jdionne@stanford.edu);

# Abstract

Identifying pathogens in complex, multi-cellular samples such as blood, urine, mucus, and wastewater is critical to detect active infection and to inform optimal treatment of human and environmental health. Surface-enhanced Raman spectroscopy (SERS) and machine learning (ML) can distinguish multiple pathogen species and strains, but processing complex fluid samples to sensitively and specifically detect pathogens remains an outstanding challenge. Here, we develop an acoustic bioprinting platform to digitize samples into millions of droplets, each containing just a few cells, which are then identified with SERS and ML. As a proof of concept, we focus on bacterial bloodstream infections. We demonstrate rapid, kHz-rate printing of  $\sim 2$ pL droplets from solutions containing *S. epidermidis*, *E. coli*, and mouse red blood cells (RBCs); when mixed with gold nanorods (GNRs), SERS enhancements of up to 1500x are achieved. With this improved signal-to-noise, we train an ML model on droplets consisting of either pure cells or mixed, multicellular species. We achieve  $\geq 99\%$  classification accuracy of droplets printed from cellularly-pure samples, and  $\geq 87\%$  accuracy in droplets printed from cellularly-mixed samples. We also determine the most significant SERS bands for classification and demonstrate that they correspond to biologically relevant vibrational modes within our cells. Our combined acoustic droplet ejection, SERS and ML platform could enable clinical and industrial translation of SERS-based cellular identification for rapid pathogen detection.

# Main

Reliable detection and identification of microorganisms is crucial for medical diagnostics, environmental monitoring, food production, biodefense, biomanufacturing, and pharmaceutical development. Such samples typically contain as few as 1-100 colony-forming units (CFU)/mL[1–3]. Though *in vitro* liquid culturing is typically used for pathogen detection, it is estimated that less than 2% of all bacteria can be readily cultured using current laboratory protocols. Further, amongst that 2%, culturing can take hours to days depending on the bacterial species [4–7]. In the case of diagnostics, broad spectrum antibiotics are often administered while waiting for culture results, leading to an alarming rise in antibiotic resistant bacteria[8]. We postulate that culture-free methods to detect pathogens in complex, multi-cellular samples might be possible by first digitizing samples into single-to-few-cellular droplets with bioprinting, then rapidly interrogating each droplet with Raman spectroscopy, and finally classifying the results using machine learning.

Raman spectroscopy is a label-free, vibrational spectroscopic technique that has recently emerged as a promising platform for bacterial species identification[9–12]. Since every cell species and strain has a unique molecular structure, they have a unique spectral fingerprint that can be used

for identification[10]. Compared to nucleic acid based tests such as polymerase chain reaction (PCR)[13–15] and protein based tests such as matrix-assisted laser desorption/ionization time-of-flight mass spectrometry (MALDI-TOF)[16, 17] and enzyme-linked immunoassay (ELISA)[18, 19], Raman requires minimal-to-no use of reagents or labels, with relatively low-cost equipment and the potential for amplification-free detection[20–23]. Furthermore, Raman is a non-destructive technique, with excitation laser powers low enough for living cells[24, 25] and negligible interference from water allowing for minimal sample preparation[26]. Combined with plasmonic or Mie-resonant nanoparticles, Raman signals can be enhanced on average by  $10^5$ - $10^6$ , and up to  $10^{10}$ [27–29], allowing for rapid interrogation of cells. With these advantages, Raman has been successfully applied to genetic profiling[30], protein detection[31–34], and even single molecule detection (Supplementary Note 1)[35–37].

To advance Raman spectroscopy to clinical and industrial relevance, it must be combined with facile sample preparation methods. Nominally, the millions to billions of cells in milliLiter-scale volumes found in key target samples such as blood would need to be processed within seconds. Acoustic droplet ejection (ADE) is among the most promising droplet generation platforms for biological samples. In ADE, ultrasonic waves are focused at the fluid-air interface, giving rise to radiation pressure that ejects a droplet from the surface. The diameter of the ejected droplet is inversely proportional to the frequency of the transducer, with 5 MHz and 300 MHz ultrasonic waves generating droplet diameters of 300  $\mu\text{m}$  and 5  $\mu\text{m}$ , respectively (Supplementary Fig. 1)[38, 39]. Unlike other commercial piezo or thermal inkjet printers, the size, speed, and directionality of the ADE ejected droplets are completely controlled by the sound waves without the need for a physical nozzle[38]. As a nozzle-less technology, acoustic droplet ejection has an unparalleled advantage in handling biological samples; in particular, it eliminates clogging, sample contamination, and compromised cell viability or biomarker structure due to shear forces from the nozzle. Furthermore, ADE allows for high throughput droplet generation, processing fluids at rates of up to 25,000 droplets/s or approximately 50 nL/s for a single ejector head. Micro-electromechanical system (MEMS)-based arrays of 1024 ejector heads have been previously reported, showing potential for processing volumes over 180 mL in under an hour[40] as compared with the days required by existent microfluidic cell separation methods[41]. Additionally, as this platform relies on acoustic waves, these waves can propagate through a matched coupling media with minimal loss of acoustic energy while avoiding any direct contact between the sample and the transducer. This eliminates any cross-sample contamination and maintains sterility (Supplementary Note 2).

Here, we demonstrate a novel approach for rapid pathogen identification in complex, multi-cellular samples by combining Raman spectroscopy with acoustic droplet ejection. We develop a bioprinter to allow sub-5-picoLiter droplets,

each consisting of a variety of cells printed with and without GNRs; thousands of droplets are printed within seconds (1kHz rates). We print samples of mouse red blood cells, suspended in an solution of aqueous ethylenediaminetetraacetic acid (EDTA), with spike-ins of gram-positive *Staphylococcus epidermidis* (*S. epi*) bacteria, and gram-negative *Escherichia coli* (*E. coli*), as well as gold nanorods (GNRs). Then, we collect Raman spectra from each printed droplet, using the optical signature to identify the cell constituents. We train machine-learning algorithms on samples printed from uniform cell types as well as mixed-cell samples to identify the droplet constituents. By optimizing our printing parameters, cell to nanorod concentrations, buffer solutions, and substrates, we achieve high Raman signal across cells while correctly identifying cell types in each droplet. We achieve cellular classification accuracies of  $\geq 99\%$  from single cell-line prints and  $\geq 87\%$  from mixed-pathogen samples, validated using scanning electron microscopy images of our droplets as the ‘ground truth’. Furthermore, we identify key spectral bands for classification by determining wavenumber importance and confirm that these features correspond to biologically relevant components within our cells. Our work lays a foundation for future SERS based bioprinting diagnostic platforms, paving the way for rapid, specific, sensitive, label-free, and amplification-free detection of live cells.

## Results

### Acoustic bioprinter design for picoliter cellular droplets

We built a Zinc Oxide 147 MHz transducer bonded to a quartz focusing lens with a focal distance of 3.5 mm. The transducer is encased in a stainless steel housing and mounted 3.5 mm above a machined stainless steel plate with a 1 mm diameter hole through which droplets are ejected downwards (Supplementary Fig. 2a). 200  $\mu\text{L}$  of sample solution is pipetted between the transducer and this plate to fill the 3.5 mm focal distance of the transducer. The aperture is large enough to negate any nozzle-like effects, and the fluid is held in place against the transducer and the plate through surface tension (Fig. 1a). We position a motorized, programmable xy stage 1 mm beneath this plate, allowing for patterned ejection. The setup is monitored through a stroboscopic camera mounted opposite to an LED to evaluate droplet stability and ejection (Fig. 1b, Supplementary Fig. 2b, 3a, b, 4). After first experimenting with a range of frequencies and droplet diameters (Fig. 1c, Supplementary Fig. 1), we selected our 147 MHz transducer frequency with droplet diameters of  $\sim 15 \mu\text{m}$  or  $\sim 2.15 \text{ pL}$  in volume, to match the order of magnitude of our cellular diameters. We found this volume allows us to print droplets with a number of cells in each droplet, while also maximizing Raman enhancement from GNR coating[42, 43].

We synthesized GNRs with a longitudinal plasmon resonance of 960 nm, chosen to closely overlap with our bacterial Raman spectral region (Fig. 1d, Supplementary Fig. 5, 6a, b). UV-vis absorption spectra and transmission

and scanning electron micrographs (TEM and SEM) of the gold nanorod samples confirm the strong near-infrared plasmon resonance peak and reasonable sample monodispersity (Supplementary Fig. 5). All rods were coated in sodium oleate and hexadecyl(trimethyl)ammonium bromide (CTAB), which gives them a slight positive charge[44], further increasing binding with our negatively charged bacteria[44, 45] and, to a lesser degree, the negatively charged RBCs[46, 47].

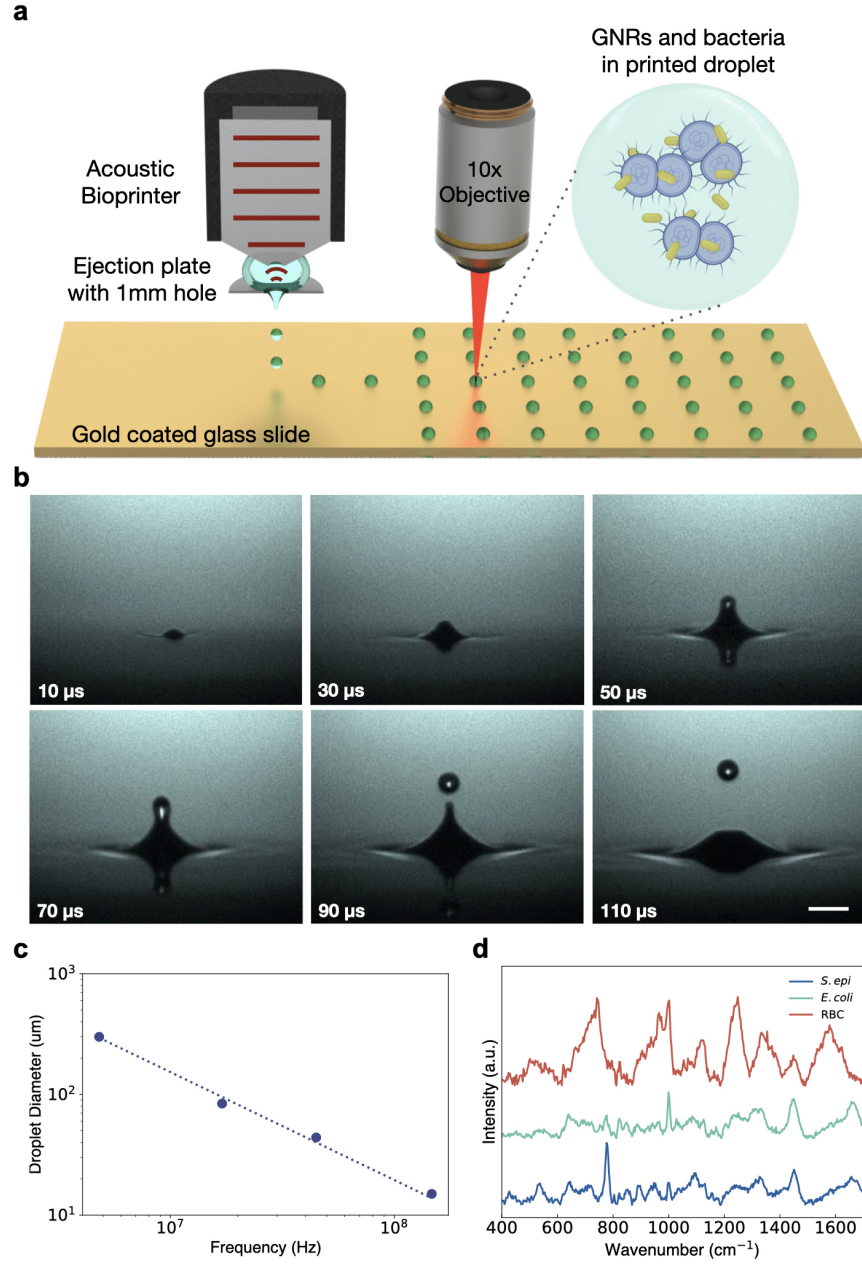


**Fig. 1** **a**, Schematic of acoustic printing platform and confocal Raman setup. Droplets containing bacteria (purple) and nanorods (gold) suspended in EDTA solution are acoustically printed onto a glass slide coated in 200 nm of gold. (see also Supplementary Fig.2, 3, 4). **b**, Stroboscopic images of the time evolution of upward droplet ejection at  $\sim 3.5\text{m/s}$  from an open pool at an acoustic frequency of 44.75 MHz and a droplet ejection repetition rate of 1kHz. Images were captured with an exposure time of 40 ms, and as such, each frame is composed of 40 droplet ejections, highlighting ejection stability. Scale bar is 100  $\mu\text{m}$ . (see also Supplementary Fig. 2). **c**, Graph of droplet diameter versus ultrasound transducer resonant frequency. Droplets were printed with 4.8 MHz, 17 MHz, 44.75 MHz, and 147 MHz and had droplet diameters of 300  $\mu\text{m}$ , 84  $\mu\text{m}$ , 44  $\mu\text{m}$ , and 15  $\mu\text{m}$  respectively, highlighting the tunability of acoustic droplet ejection. (see also Supplementary Fig.1). **d**, (d) Raman spectra of dried cellular samples, including *S. epi*, *E. coli*, and red blood cells (RBCs) on a gold coated slide.

## Stable acoustic droplet ejection of patterned, viable cellular arrays

For this study, cells were suspended in a 1:9 volumetric mixture of EDTA and deionized water, diluted to a final concentration of  $1 \times 10^9$  cells/mL. This solution was chosen to prevent hemolysis of our red blood cells (RBCs), while avoiding crystallization upon drying present in droplets printed from salt-based buffers (Supplementary Fig. 7). Furthermore, we hypothesize that the inclusion of EDTA within our solutions aggregates our GNRs into clusters with cells due to interactions with the residual CTAB on the GNRs (Supplementary Fig. 8)[48] and the surface charge on our cells, providing a denser coating of GNRs on cell surfaces with few rods located elsewhere in the droplet. Samples were printed on silane-treated, gold-coated glass substrates to minimize background spectra in the region of interest while further inducing coating of GNRs on our cells through their hydrophobicity (Supplementary Fig. 9, 10).

We can reliably and precisely print patterned grids of droplets containing bacteria and RBCs with GNRs and without GNRs, printed at ejection rates of 1 kHz, as shown in Fig. 2a. Grid prints of additional cell line mixtures can be found Supplementary Fig. 11. Furthermore, we maintain cell viability during printing as demonstrated by the positive growth of cells printed directly onto agar-coated slides. Fig. 2b, for example, shows droplets of *E. coli* bacteria grown 0, 12, 24, and 36 hours post printing, demonstrating the maintained viability of the cells after acoustic droplet ejection.

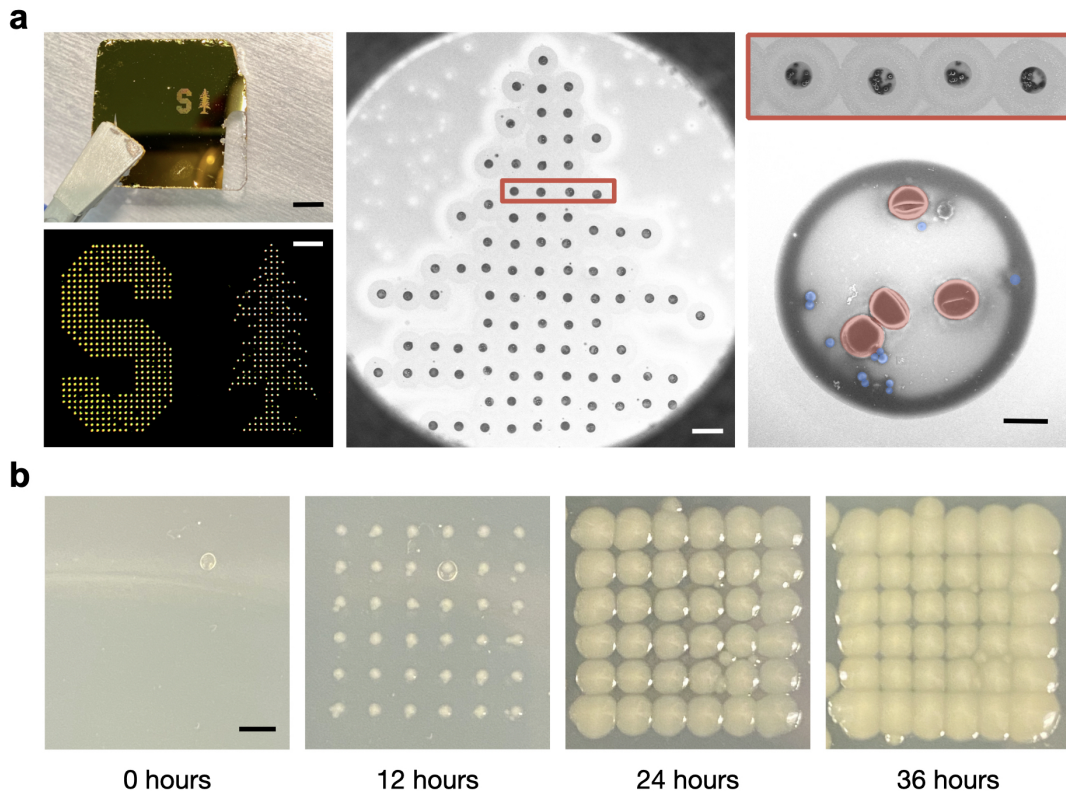


**Fig. 2 Patterned droplet ejection from cellular stock solution.** All droplets were ejected at 147 MHz. **a**, Pattern printout of droplets containing a 1:1 mixture of *S. epi* bacteria and mouse RBCs onto a gold coated slide. Image on the left shows a brightfield image (top) taken with a 5x objective lens with a scale bar of 50  $\mu\text{m}$ . The photograph (bottom) has a scale bar of 4 mm. Middle, SEM of the top portion of the tree region of the print with a scale bar of 100  $\mu\text{m}$ . Right shows a single row of 4 droplets from the large area print, and then a magnified image of a single droplet with false coloring showing RBCs in red and *S. epi* bacteria in blue. Scale bar is 5  $\mu\text{m}$ . **b**, Droplets containing *E. coli* bacteria were printed onto an agar coated slide and incubated at 37°C for upto 36 hours to demonstrate cellular viability of printed samples. 100 droplets were placed at each location to ensure each droplet contained cells. Scale bar is 2 mm.

### Single cell-line droplet SERS-based classification

SERS spectra from our acoustically-printed droplets are collected using a 785 nm laser (Supplementary Fig. 12). We first print grids of droplets from 6 cellularly-pure samples: *S. epi*, *S. epi* with GNRs, *E. coli*, *E. coli* with GNRs, mouse RBCs, and mouse RBCs with GNRs (Fig. 3a, Supplementary Fig. 11). Fig. 3b shows a magnified SEM of the droplet printed with *S. Epi* and GNRs and demonstrates that our cells are abundantly coated with GNRs. The normalized, average signal from 100 droplets of each cellular sample with GNRs and average signal from 15 droplets of each sample without GNRs are shown in Fig. 3c, with spectral acquisition times of 15 s for each droplet (Supplementary Fig. 13, 14, 15, 16). Note that little to no signal is observed with this collection for droplets without the nanorods. Relative signal intensities for non-normalized samples with data standard deviations can be found in Supplementary Fig. 17. The data shows significant Raman signal enhancement

from the sample sets with nanorods compared to the controls, estimated at between 300 - 1500x. For more precise classification of our droplet mixtures, we start by reducing the dimensionality of our spectra from 508 wavenumbers to 24 components using PCA in order to prevent classifier oversampling due to our dataset having more features than samples. We show that the first 24 principal components account for  $>90\%$  of our sample variance (Supplementary Fig. 18), and we still see clear sample differentiation between each dataset and cell type on a 2-component t-distributed stochastic neighbor embedding projection (t-SNE) after PCA (Fig. 3d, Supplementary Fig. 19). We then use a random forest classifier for our multiclass analysis from our complex samples. We tune our classifier hyperparameters using a cross-validated grid search to generate optimized parameters. Inputting these parameters into our classifier, we take 100 spectra from each of our 3 classes of cellular samples with GNRs and perform a stratified K-fold cross validation of our classifier’s performance across 10 splits and demonstrate  $\geq 99\%$  classification accuracy across all samples (Fig. 3e).

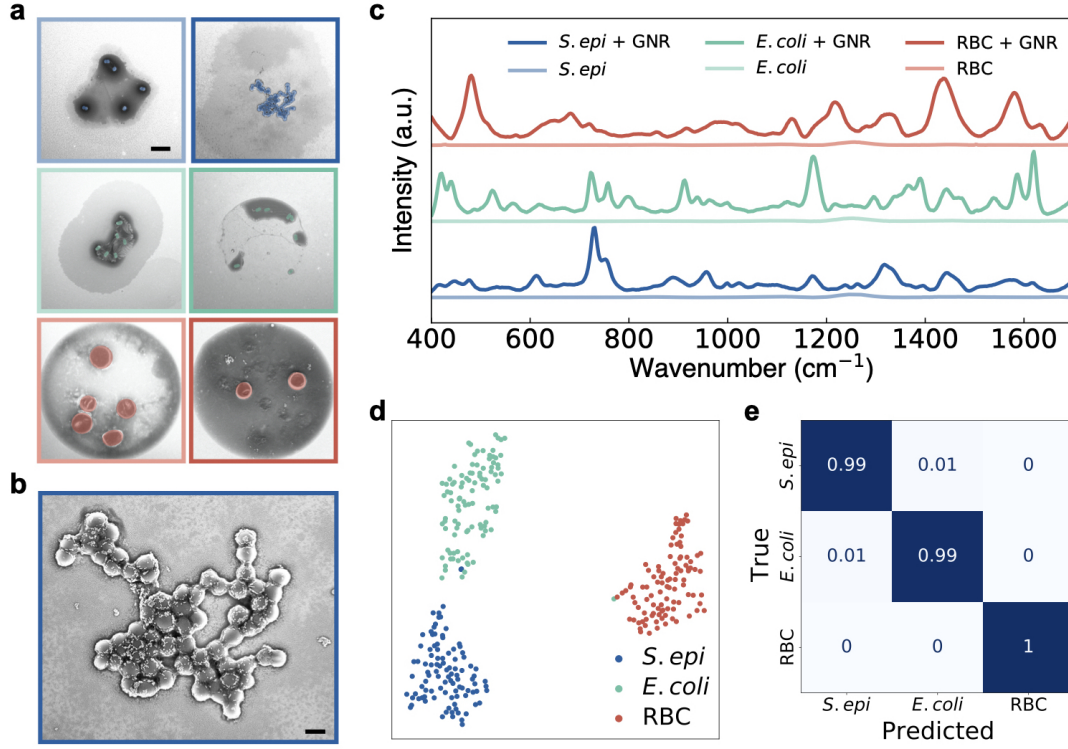


**Fig. 3 Spectral identification of cells printed with GNRs.** **a**, SEMs showing single droplets printed from varying cellular samples suspended in our EDTA solution at a concentration of  $1e9$  cells/mL. Left column shows samples without GNRs, and the right column shows cells printed with GNRs. From top to bottom, droplets contain: *S. epi*, *E. coli*, and RBCs with false coloring added to highlight the cells. The scale bar is  $5\ \mu\text{m}$ . **b**, Magnified SEM of a droplet containing *S. epi* coated with GNRs from Fig. 3a. SEM highlights that the bacteria are coated with GNRs with very few rods dispersed in the rest of the droplet. Scale bar  $2\ \mu\text{m}$ . **c**, Mean SERS spectra of 100 measurements each taken from single droplets printed from three cell lines (*S. epi*, *E. coli*, and RBCs) mixed with GNRs. **d**, 2-component t-SNE projection across all 300 Raman spectra acquired from droplets printed with GNRs. Data is plotted after performing a 24-component PCA for dimensionality reduction. Plots show distinct clustering of our cell lines. **e**, Normalized confusion matrix generated using a random forest classifier on the 300 spectra collected from single cell-line droplets of *S. epi*, *E. coli*, and mouse RBCs mixed with GNRs. Samples were evaluated by performing a stratified K-fold cross validation of our classifier's performance across 10 splits, showing  $\geq 99\%$  classification accuracy across all samples.

## Multi-cellular droplet classification and Raman feature importance

We demonstrate that we can accurately classify droplets printed at 147 MHz from complex, clinically-relevant cellular mixtures. We print arrays of droplets from  $200\ \mu\text{L}$  of solution formed from equal mixtures of *S. epi* and RBCs, *E. coli* and RBCs, and *S. epi*, *E. coli*, and RBCs, all diluted to a final concentration of  $1e9$  cells/mL of each cell type in our aqueous EDTA solution and mixed with GNRs (Fig. 4a). We collect single-droplet SERS spectra from our mixture printouts, identically to that of our single cell-line droplets, using a 785 nm laser with a 15 s acquisition time. We then evaluate 100 spectra each of all six classes of our samples, the three single-cellular samples presented in Fig. 3

and our 3 mixture classes. We reduce the dimensionality of our samples to 30 components using PCA, sufficient to account for  $>90\%$  of our sample variance (Supplementary Fig. 20), and plot a 2-component t-SNE projection to show clear clustering between each dataset (Fig. 4b, Supplementary Fig. 21). We then re-tune our classifier hyperparameters with our new data, evaluate our samples using a random forest classifier with a stratified K-fold cross-validation as previously described, and demonstrate  $\geq 87\%$  classification accuracy across all samples (Fig. 4c).

To verify that our classifier is using physiologically meaningful spectral bands for prediction, we compute the feature importance at each wavenumber and validate that high importance bands correspond to specific biological components and vibrations in our cells. To identify these meaningful bands, we start by repeatedly splitting our 600 spectra into random 80:20 train/test splits and train a model on each training set. For the test set, we iterate through the wavenumbers and at each iteration, perturb the spectrum by modulating the amplitude with a Voigt distribution. After each perturbation, we recalculate the classification accuracy, compare the updated results with our baseline accuracy, and determine the importance for each wavenumber - the greater the decrease in accuracy due to our perturbation, the more important the wavenumber. We split our samples using a stratified shuffle split and repeat 10 times. Each wavenumber of each spectrum in the test set is perturbed 5 times and all results are averaged to determine our final feature importance. We plot a heatmap highlighting the relative wavenumber importance overlaid with a plot of the mean and standard deviation of the perturbed classification accuracy (Fig. 4d, Supplementary Fig. 22, 23). We further plot the normalized, average signal from 100 droplets of each cellular sample with GNRs. Relative signal intensities for non-normalized samples with data standard deviations can be found in Supplementary Fig. 24. We note that the key spectral bands highlighted by our algorithm match peaks in our spectra and that these distinct peak wavenumbers represent bands previously reported in literature of dried and liquid SERS of our cell-lines including *S. epi*, *E. coli*, and RBCs (Fig. 4e, Supplementary Fig. 25)[44, 49–59]. We specifically note that peaks at  $732.5$  and  $1330\text{ cm}^{-1}$  from our *S. epi*-containing samples are attributed to purine ring-breathing modes[54] and the Adenine part of the flavin derivatives or glycosidic ring mode of polysaccharides[53]; peaks at  $755$  and  $1450\text{ cm}^{-1}$  from our *E. coli*-containing samples are attributed to Tryptophan ring breathing[59] and  $\text{CH}_2/\text{CH}_3$  deformation of proteins and lipids[51]; and peaks at  $482$  and  $1224\text{ cm}^{-1}$  from our RBC-containing samples are attributed to  $\gamma 12$  out of plane deformation of porphyrin, a main component of hemoglobin[56], and  $\nu 13$  or  $\nu 42$  valence[57]. Further peak assignments can be found in Supplementary Table 1.

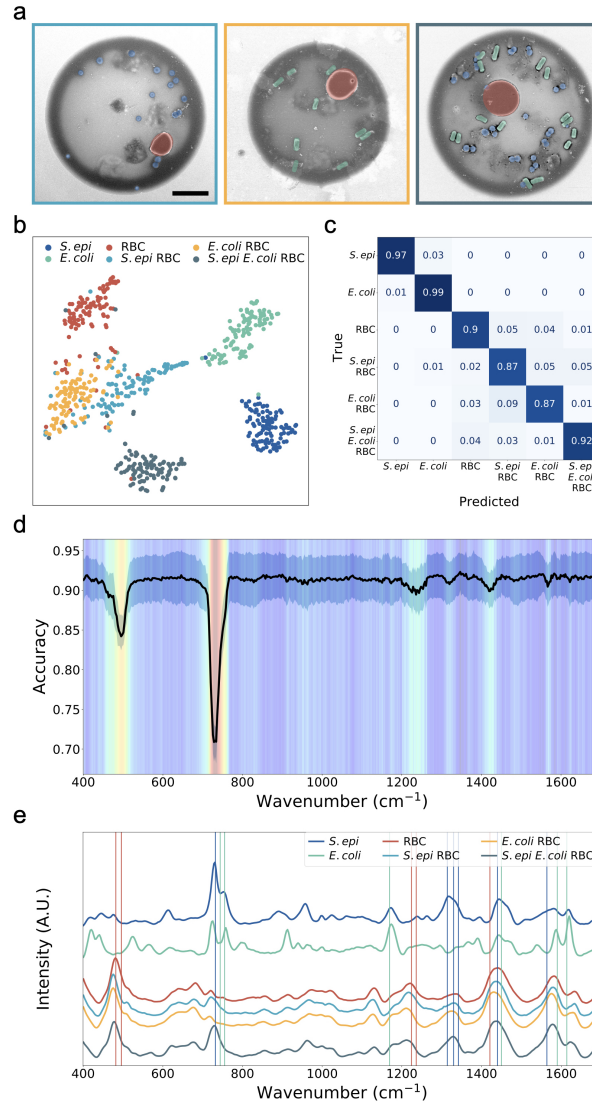


**Fig. 4** **a**, False-color SEMs of droplets printed from (left to right): an equal mixture of *S. epi* bacteria and RBCs, *E. coli* bacteria and RBCs, and *S. epi*, *E. coli*, and RBCs all diluted to  $1 \times 10^9$  cells/mL in aqueous EDTA and mixed with GNRs. The scale bar is  $5 \mu\text{m}$ . **b**, 2-component t-SNE projection across all 600 Raman spectra acquired from 100 droplet measurements each, taken from single droplets printed from three cell lines (*S. epi*, *E. coli*, and RBCs) and three mixtures (*S. epi* and RBCs, *E. coli* and RBCs, and *S. epi*, *E. coli*, and RBCs) mixed with GNRs. Data is plotted after performing a 30-component PCA for dimensionality reduction. Plots show clustering of our cell lines with the most overlap between droplet mixture samples. **c**, Normalized confusion matrix generated using a random forest classifier on the 600 spectra collected from single cell-line droplets of *S. epi*, *E. coli*, and mouse RBCs mixed with GNRs, and our 3 cell mixtures. Samples were evaluated by performing a stratified K-fold cross validation of our classifier's performance across 10 splits, showing  $\geq 87\%$  classification accuracy across all samples. **d**, Heatmap highlighting feature extraction performed to determine relative weight of spectral wavenumbers in our Random Forest classification. Heatmap is overlaid with a plot of the mean and standard deviation of the classification accuracy (black) calculated across all trials. Wavenumbers with lower accuracies are shown to be critical features as random perturbations are highly correlated with decreases in classification accuracy. **e**, Plot of the mean SERS spectra of 100 measurements each, taken from single droplets printed from three cell lines (*S. epi*, *E. coli*, and RBCs) and three mixtures (*S. epi* and RBCs, *E. coli* and RBCs, and *S. epi*, *E. coli*, and RBCs) mixed with GNRs. Wavenumbers reporting to biological peaks found in SERS spectra of *S. epi*, *E. coli*, and RBCs are plotted as blue, green, and red vertical lines, respectively. Peak assignments can be found in Supplementary Table 1.

## Discussion

We have demonstrated a rapid platform for acoustic printing-based droplet SERS of biological samples. Our system enables rapid digitization of cells from fluid samples in picoliter droplets with minimal sample contamination through nozzle-free acoustic printing at kilohertz ejection rates. As a result of our choice in printer frequency, cell stock solution, and slide surface treatment, our platform generates droplets containing cells uniformly coated in GNRs. Our results show that we can stably print samples of cells with and without GNRs and can demonstrate clear signal enhancements of up to 1500x from the addition of our GNRs. Furthermore, from these droplets, we demonstrate single-droplet Raman interrogation and cellular identification in 15 seconds. We show that we generate these consistent Raman spectra from gram-positive and gram-negative bacteria as well as from RBCs and can differentiate spectra. Finally, we demonstrate that we can identify distinct cell types present in droplets printed from a mixture of cell lines using machine learning algorithms.

Our work could advance Raman-based clinical research, clinical diagnostics, and disease management. Minimally invasive, fluid-based biomarker detection is gaining traction for the development of new point-of-care systems. A reliable and automated biological acoustic printer coupled with SERS nanoparticles and Raman spectroscopy could be used to separate, count, and identify various cell lines allowing for rapid, specific, and label-free cellular analysis. Furthermore, ADE-based SERS could be designed with an array of ejector heads to rapidly split large patient sample volumes, or a single-ejector could provide detailed analysis of a small volume, minimizing the use of expensive reagents. As such, ADE-based SERS could enable culture-free cellular identification and monitoring from samples with low concentrations or from samples with species that are difficult to culture, including circulating tumor cells (CTCs) for cancer screening and monitoring[60–62], CD4 levels for HIV monitoring[60, 63], and strain specific identification of slow-growing *Mycobacterium tuberculosis* for treatment planning[64–66]. Additionally, given that acoustic printing is nozzle-free and contactless, ADE-based SERS could facilitate easy multiplexing of various patient samples or other relevant media as the ejector can easily scan across a number of different sample wells without risking contamination. Lastly, given the versatility of our substrates, colloidal GNRs, and printing platform, our system is not limited to processing cells but could easily be modified for use in detecting other biomarkers including small molecules and proteins, coupled with surface chemistry for labeled detection of nucleic acids, and used for low-volume interrogation of pharmaceutical samples in drug-development. Our work in integrating SERS cellular interrogation with acoustic bioprinting and machine learning provides a foundation for further research into rapid, cellular-based diagnostics, and paves the way for reliable, low-cost point-of-care diagnostics.

# Methods

## Gold nanorod synthesis and characterization

Hexadecyl(trimethyl)ammonium bromide (CTAB) and sodium oleate (NAOL) coated gold nanorods were synthesized following previously described protocols[67]. The nanorods were cleaned by centrifuging 1.5 mL aliquots twice at (9000 rpm, 20 min), allowing for one wash after synthesis as this has been shown to be adequate to maintain cell viability while preventing nanorod aggregation[44]. Samples were concentrated down to 10  $\mu$ L to be mixed with cell samples and diluted to a final volume of 200  $\mu$ L. Absorption spectra were recorded using a Cary 5000 UV-vis-NIR spectrometer. Scanning electron microscopy images were taken using FEI Magellan 400 XHR Scanning Electron Microscope (SEM). Transmission electron microscopy images were taken using FEI Tecnai G2 F20 X-TWIN Transmission Electron Microscope (TEM).

## Scanning electron microscopy (SEM) of printed samples

For scanning electron microscope (SEM) imaging, printed samples were imaged after completion of all Raman Spectroscopy. Samples were prepared by evaporating a  $\sim$ 10 nm layer of 60:40 gold to palladium to allow for better visualization of cells under electron beam illumination. SEM images were taken using FEI Magellan 400 XHR Scanning Electron Microscope.

## Bacteria culturing and preparation

*E. coli*, ATCC 25922, and *S. epidermidis*, ATCC 12228, were grown from frozen stocks on Trypticase Soy Agar 5% Sheep Blood 221239 BD plates. A single colony was seeded in 10 mL Lysogeny broth (LB) culture medium and incubated at 37°C shaking at 300 rpm for 15 hrs using Thermo Scientific MaxQ 4450 incubator. 1.5 mL of culture was washed with water three times at 6000 rpm for 3 min using a mySPINTM 6 Mini Centrifuge. Samples were then concentrated down to 100  $\mu$ L volumes. The cell count was collected using a Bright-Line Hemacytometer using a 1:5000 dilution of the cell culture stock solution. Stock solutions contained on average  $\sim$ 1e10 cells/mL.

## Preparation of red blood cell solutions

CD-1 (1CR) purified Mouse Red Blood Cells (RBCs) from pooled samples treated with K2EDTA, MSE00RBK2-0104095, were purchased from BioIVT in 5mL volumes. RBCs were diluted in a 1:9 v/v mixture of Invitrogen UltraPure 0.5 M EDTA, Invitrogen 15575020, to a final dilution of 1:5000 and cell counts were collected using a Nexcelom Cellometer X2 cell counter.

## Preparation of mixtures for printing

Printing was completed using 200  $\mu$ L of solution. All samples were diluted to a final volume of 200  $\mu$ L in a 1:9 v/v mixture of Invitrogen UltraPure 0.5 M

EDTA, Invitrogen 15575020, and Millipore water, unless otherwise noted. For samples with cells and no nanorods, a single concentrated cell solution or a mixture of cell solutions was diluted in aqueous EDTA to a final concentration of  $1 \times 10^9$  cells/mL of each cell type in a given mixture. This concentration was chosen to ensure a majority of printed droplets contained at least 1 cell. For samples of cells mixed with nanorods, cleaned, concentrated nanorod solution was first mixed with concentrated cell stock solution, for our final concentration of  $1 \times 10^9$  cells/mL per cell type, and then subsequently diluted with our aqueous EDTA solution. All solutions are mixed by inverting our microcentrifuge tubes a minimum of 10 times.

EDTA was chosen as our sample buffer to avoid crystallization upon drying seen with PBS (Supplementary Fig. 6). On top of that, EDTA provides two further advantages for our printed samples. When EDTA-containing droplets dry on a hydrophobic substrate, a central region of aggregated EDTA, cells, and GNRs dries in a much smaller area than that of a full droplet, forcing the cells and GNRs into a much smaller volume, ensuring better coverage of the cells with GNRs (Supplementary Fig. 9). Furthermore, the EDTA induces aggregation among the GNRs due to the electrostatic interaction between any residual CTAB on our GNRs and the EDTA [48], as demonstrated in Supplementary Fig. 7. We hypothesize that this clustering, when coupled with the addition of cells, allowed for greater quantities of nanorods to coat the cells, and led to the creation of SERS “hot spots” amongst the aggregated GNRs, providing strong enhancements [42, 68].

Finally, we show that the addition of the EDTA and nanorods adds minimal Raman background noise (Supplementary Fig. 8, 9, 14), making it appropriate for our work in Raman cellular identification. Finally, to further minimize coffee-ring effects from nanorods upon droplet drying, we used vapor deposition to coat our gold-coated slides with a hydrophobic silane layer (3-Aminopropyl)triethoxysilane (APTMS) which allows for a more close packing of our GNRs, providing greater and more uniform enhancement on our cells [69–71].

## **Fabrication of silanized, gold-coated glass slides**

The gold substrates used in this work were prepared by evaporating a 5 nm adhesion layer of titanium, followed by 200 nm of gold at a rate of 1 Å/second using a KJ LEsger e-beam evaporator onto piranha cleaned borosilicate glass slides. The gold-coated glass slides were then cleaned with an oxygen plasma, using a Diener Pico Oxygen Plasma Cleaner, for 3 min at 100 W power and  $\sim 2$  mbar of pressure, and silanized with 3-(aminopropyl)trimethoxysilane, APTMS, using vapor deposition in order to make the surface more hydrophobic and allow for greater aggregation of the gold nanorods on the cells [71–73]. Slides were placed in a 1 liter flask in the presence of 100  $\mu$ L of APTMS, Sigma-Aldrich 281778-5ML. The flask was then placed in a water bath at 40°C and allowed to react for 1 hr, after which the slides were removed from the flask and placed on a hot plate heated to

40°C for 10 min to allow for the evaporation of loosely bound molecules. We demonstrate that this APTMS layer also provides minimal Raman background noise, making it a great candidate for quick and easy substrate modification for biological Raman analysis (Supplementary Fig. 8).

## Acoustic printing

Acoustic printing was completed using our custom-built ultrasonic, immersion transducer with a center frequency of 147 MHz and a focal distance of 3.5 mm (unless otherwise noted) as determined using a network analyzer, Hewlett Packard 8751A, and through pulse echo measurements taken on an oscilloscope, Keysight InfiniiVision DSOX3054A. The transducer was bound to a quartz, spherical focusing lens. The transducer was mounted on x,y,z manual translation stages, facing downwards, held 3.5 mm above a 303 stainless steel ejection plate with a 1 mm hole. For printing experiments, fluid was pipetted into the gap between the tip of the focusing lens and the ejection plate, held in place through surface tension. During printing experiments, droplets were ejected downwards through this 1 mm hole onto our chosen substrates (Supplementary Fig. 2).

To generate our droplets, our transducer was powered by a waveform generator, Keysight 33600A Series Trueform Waveform Generator. The waveform generator was connected to a synthesized RF signal generator, Fluke 6062A, which in turn is connected to a power amplifier, Minicircuits ZHL-03-5WF+. Our waveform generator produces a square-wave burst with a repetition frequency of 1 kHz, when operating continuously, at our desired pulse width of 5.5  $\mu$ s and at a voltage of 1.5 volts, enough to trigger our RF synthesizer. The RF synthesizer generates a sinusoidal wave at 147 MHz and at our desired voltage, which then gets amplified before reaching the transducer. Droplets printed from deionized water were ejected with 0.096  $\mu$ J of energy, droplets printed from samples of *S. epi* and *E. coli* with and without GNRs were printed with 0.139  $\mu$ J of energy, and droplets printed with RBCs with and without GNRs and from mixtures of RBCs, *S. epi*, *E. coli*, and GNRs were all printed with 0.386  $\mu$ J of energy.

To ensure stable ejection, we monitored ejection using a camera, Allied Vision Guppy Pro F-125 1/3" CCD Monochrome Camera, coupled with a 20x objective pointed at the bottom of our ejection plate. This camera was mounted opposite a strobing LED, also triggered by our waveform generator. We also monitored the acoustic echo using an inline oscilloscope, Keysight InfiniiVision DSOX3054A. To set up our printer, we pipette in 200  $\mu$ L of fluid, turn on power to our transducer, and ensure that the transducer is in focus by manually adjusting the focal distance of our transducer until we maximize the echo as observed on the oscilloscope. We then vary the output voltage of the RF synthesizer until we stably eject a single droplet without any additional satellite droplets, as observed through our camera feed. We were then ready to pattern print arrays of droplets (Supplementary Fig. 3, 4).

## Pattern printing

Pattern printing was completed using a custom 3D printed substrate holder mounted to two perpendicularly stacked Thorlabs DDS100M 100mm brushless DC linear translation stages controlled by two Thorlabs K-Cube brushless DC servo drivers. Our substrate is mounted  $\sim 1$  mm below our ejection plate to minimize droplet translation before it reaches the substrate. A MATLAB, Mathworks, 2018b, script was used to pattern print droplets onto our substrate by controlling both our motorized stages and our waveform generator to trigger droplet ejection at specific substrate locations.

## Raman spectroscopy

Raman spectra was collected using the Horiba XploRa confocal Raman microscope. The excitation wavelength for all measurements was 785 nm. The Raman shift from  $400\text{ cm}^{-1}$  to  $2000\text{ cm}^{-1}$  was collected using 600 gr/mm grating. For baseline Raman spectra shown in Fig. 1, laser light was directed to and Raman scattered light was collected from the sample using a 100x LWD, 0.6 NA objective with spot size of  $0.83\text{ }\mu\text{m}$ , with laser power at the sample of  $\sim 6.71\text{ mW}$ , and acquisition time of 180 s. For spectra collected from each entire droplet, laser light was directed to and Raman scattered light was collected from the sample using a 10x, 0.25 NA objective with spot size of  $2\text{ }\mu\text{m}$ , with laser power at the sample of  $\sim 10.6\text{ mW}$ , and acquisition time of 15 s (Supplementary Fig. 11). Bacterial NR mixtures were measured within  $\sim 2$  hr of sample preparation.

## Spectral data processing

Python (Jupyter Notebook) was used to process spectral data. For spectra pre-processing, samples were first thresholded to a minimum intensity of 150 a.u. to remove any spectra with weak signal that likely were collected on the substrate without the presence of cells. We then transformed our data by taking  $\log_{10}(y)$  [74, 75] and smoothed the spectra using wavelet denoising [76, 77]. To perform our smoothing, we used the *denoise\_wavelet* function from the scikit-image Python library: `denoise_wavelet(y, method='BayesShrink', mode='soft', wavelet_levels=1, wavelet='coif3', rescale_sigma=True)`. We then performed a baseline removal by using a polynomial fit with degree 10. The specific package used and code line is: `peakutils.baseline(y, deg=10, max_it=1000, tol=0.0001)`. Note, the need for a higher degree polynomial arises from a typical instrumental background that is difficult to fit with lower degree fits. Following this baseline correction, Spectra were then individually normalized across all wavenumbers by subtracting the spectral mean and dividing by the standard deviation using the NumPy Python library [78], where *y* is the array of intensity values across all wavenumbers for each spectra:  $(y - \text{numpy.mean}(y))/\text{numpy.std}(y)$  (Supplementary Fig. 26).

For classification of samples, we further pre-process data by reducing dimensionality of our spectra from 508 to the number of components necessary to account for 90% of our sample variance using the PCA algorithm from Scikit-learn[79] (Supplementary Fig. 18, 20). Classification was performed using a Random Forest Classifier. We first tuned our classifier hyperparameters using a cross-validated grid search to generate optimized parameters. To do this we use Scikit-learn *StratifiedShuffleSplit*[79] function to randomly split our sample 20 times into an 80:20 train:test split and created a parameter grid for our number of estimators: {50, 100, 150, 200, 250, 300}, max features: {auto, sqrt, log2}, and max depth: {2, 5, 10, 15, 20}. We created our Random Forest Classifier using Scikit-learn, with a min\_samples\_split=2, and then performed our grid search using Scikit-learn *GridSearchCV*, with refit = True, n\_jobs = 3, and verbose = 190. We then perform a stratified K-fold cross validation (Scikit-learn *StratifiedKFold*[79] with shuffle=True) of our classifier’s performance across 10 splits using these optimal parameters. Finally, we use the Scikit-learn *confusion\_matrix*[79] function to plot our results. Intermediate t-SNE projections were plotted using Scikit-learn *manifold.TSNE* with a perplexity = 10[79] (Supplementary Fig. 19, 21).

Raman wavenumber importance was performed using Voigt profile perturbation across all spectral wavenumbers. To achieve this, all spectra were first preprocessed as described above. Our spectra of interest (600 spectra across all 6 cellular classes) were partitioned into an 80:20 train/test split using Scikit-learn *StratifiedShuffleSplit*[79] with 10 splits. We reduce the dimensionality of our training set to 10 components using the PCA algorithm from the Scikit-learn[79]. We train our Random Forest Classifier on our training spectra using optimized hyperparameters determined using a cross-validated grid search as previously described. We iteratively perturb our test set at each wavenumber to determine the relative importance of each wavenumber to accurate spectra classification. To do this, we iterate over each wavenumber in each normalized spectrum in our test set (120 spectra per split). For each wavenumber, we perturb our test spectra with a Voigt profile curve[80, 81], varying the intensity of the Voigt function 5 times at each wavenumber for each spectrum to get a large sample set. To generate our Voigt profiles, we first take all spectra in our entire sample set (600 spectra) and shift the intensity at a given wavelength ( $w$ ) to guarantee that the intensities are positive. We then randomly shuffle all intensities and randomly select one to be used to generate our Voigt profile (voigt\_intensity). We generate this profile with our half-width at half-maximum (HWHM) of the Lorentzian profile,  $\gamma = 2$ , and the standard deviation of the Gaussian profile,  $\sigma = \alpha / \text{np.sqrt}(2 * \text{np.log}(2))$ , where  $\alpha = 5$ . From here, we create our voigt\_profile =  $\text{np.real}(\text{wofz}((x - w + 1j * \gamma) / \sigma / \text{np.sqrt}(2))) / \sigma / \text{np.sqrt}(2 * \text{np.pi})$ , where  $x$  is the entire range of wavenumbers, and scale this distribution to range from [0,1]. We utilize the *wofz* function from the SciPy Python library to implement the Faddeeva function as the Voigt profile is related to the real part of the Faddeeva function. We also utilize various mathematical functions from the NumPy Python library to generate our profile.

Voigt profile width was chosen to match peak widths seen in our spectra. To perturb our spectra with this profile, we take each spectra and shift intensities by the minimum, so that all intensities are positive (`pos_spectrum`). We then perturb each wavenumber by our Voigt profile to generate a modified spectrum = `pos_spectrum*(1-voigt_profile) + voigt_intensity*voigt_profile`. We transform this perturbed spectrum with our established PCA and classify it using our trained Random Forest Classifier. We then plot a confusion matrix for each wavenumber using Scikit-learn *confusion\_matrix*[79] and generate an accuracy and f1 score using Scikit-learn *classification\_report*[79], across all 6000 trials per wavenumber. Finally, we use our confusion matrix to generate the per class performance. See Supplementary Fig. 19 for more.

## Competing interests

The authors declare no competing financial interests.

## Acknowledgments

The authors gratefully acknowledge funding from the Stanford Catalyst for Collaborative Solutions (funding ID 132114), the Chan Zuckerberg Biohub Investigator Program, the NIH-NCATS-CTSA (Grant number UL1TR003142), the Gates Foundation (OPP 1113682), the National Science Foundation (grant number 1905209), the NIH New Innovator Award (1DP2AI152072-01), and from seed funds from the Stanford Center for Innovation in Global Health. Part of this work was performed at the Stanford Nano Shared Facilities (SNSF) and the Soft & Hybrid Materials Facility (SMF) which are supported by the National Science Foundation and National Nanotechnology Coordinated Infrastructure under awards ECCS-2026822 and ECCS-1542152. The authors also thank Dr. Jack Hu for help with gold-coating substrates, Babatunde Ogunlade for help with piranha cleaning substrates, Rich Chin and Dr. Juliet Jamtgaard for assistance with SEM sample coating, and Hongquan Li, Dr. Jack Hu, Dr. Halleh Balch, Dr. Jeong Kim, and Shoaib Meenai for insightful discussions.

## Author Contributions

F.S., L.T., A.A.E.S., B.K-Y., and J.A.D. conceived and designed the experiments. F.S., K.F., A.A.E.S, and B.K-Y. designed, developed, and characterized the acoustic bioprinter. F.S. synthesized the gold nanorods, cultured the cells, printed samples, and collected Raman spectra of printed droplets. N.V. and F. S. wrote and implemented algorithms for spectral data pre-processing and classification. J.A.D., A.A.E.S, and B.K-Y supervised the project along with S.S.J and N.B. on relevant portions of the research. All authors contributed to the preparation of the manuscript.

## References

- [1] Kreger, B. E., Craven, D. E., Carling, P. C. & McCabe, W. R. Gram-negative bacteremia. III. reassessment of etiology, epidemiology and ecology in 612 patients. *Am. J. Med.* **68** (3), 332–343 (1980) .
- [2] Werner, A. S., Glenn Cobbs, C., Kaye, D. & Hook, E. W. Studies on the bacteremia of bacterial endocarditis. *JAMA* **202** (3), 199–203 (1967) .
- [3] Gordon, M. A. *et al.* Invasive non-typhoid salmonellae establish systemic intracellular infection in HIV-infected adults: an emerging disease pathogenesis. *Clin. Infect. Dis.* **50** (7), 953–962 (2010) .
- [4] Wade, W. Unculturable bacteria—the uncharacterized organisms that cause oral infections. *J. R. Soc. Med.* **95** (2), 81–83 (2002) .
- [5] Bodor, A. *et al.* Challenges of unculturable bacteria: environmental perspectives. *Rev. Environ. Sci. Technol.* **19** (1), 1–22 (2020) .
- [6] Hahn, M. W., Koll, U. & Schmidt, J. in *Isolation and cultivation of bacteria* (ed. Hurst, C. J.) *The Structure and Function of Aquatic Microbial Communities* 313–351 (Springer International Publishing, Cham, 2019).
- [7] Pedrós-Alió, C. & Manrubia, S. The vast unknown microbial biosphere. *Proc. Natl. Acad. Sci. U. S. A.* **113** (24), 6585–6587 (2016) .
- [8] Fleischmann, C. *et al.* Assessment of global incidence and mortality of hospital-treated sepsis. current estimates and limitations. *Am. J. Respir. Crit. Care Med.* **193** (3), 259–272 (2016) .
- [9] Bantz, K. C. *et al.* Recent progress in SERS biosensing. *Phys. Chem. Chem. Phys.* **13** (24), 11551–11567 (2011) .
- [10] Ho, C.-S. *et al.* Rapid identification of pathogenic bacteria using raman spectroscopy and deep learning. *Nat. Commun.* **10** (1), 1–8 (2019) .
- [11] Tian, T. *et al.* Self-assembled plasmonic nanoarrays for enhanced bacterial identification and discrimination. *Biosensors and Bioelectronics* **197**, 113778 (2022) .
- [12] Tadesse, L. F. *et al.* Toward rapid infectious disease diagnosis with advances in surface-enhanced raman spectroscopy. *J. Chem. Phys.* **152** (24), 240902 (2020) .
- [13] Hoshino, T. *et al.* PCR detection and identification of oral streptococci in saliva samples using gtf genes. *Diagn. Microbiol. Infect. Dis.* **48** (3), 195–199 (2004) .

- [14] Rodriguez-Lázaro, D., Hernández, M., Esteve, T., Hoorfar, J. & Pla, M. A rapid and direct real time PCR-based method for identification of salmonella spp. *J. Microbiol. Methods* **54** (3), 381–390 (2003) .
- [15] Greisen, K., Loeffelholz, M., Purohit, A. & Leong, D. PCR primers and probes for the 16S rRNA gene of most species of pathogenic bacteria, including bacteria found in cerebrospinal fluid. *J. Clin. Microbiol.* **32** (2), 335–351 (1994) .
- [16] Tsuchida, S., Umemura, H. & Nakayama, T. Current status of Matrix-Assisted laser Desorption/Ionization-Time-of-Flight mass spectrometry (MALDI-TOF MS) in clinical diagnostic microbiology. *Molecules* **25** (20) (2020) .
- [17] Luethy, P. M. & Johnson, J. K. The use of Matrix-Assisted laser Desorption/Ionization Time-of-Flight mass spectrometry (MALDI-TOF MS) for the identification of pathogens causing sepsis. *J Appl Lab Med* **3** (4), 675–685 (2019) .
- [18] Dylla, B. L., Vetter, E. A., Hughes, J. G. & Cockerill, F. R., 3rd. Evaluation of an immunoassay for direct detection of escherichia coli O157 in stool specimens. *J. Clin. Microbiol.* **33** (1), 222–224 (1995) .
- [19] Sandström, G. E., Wolf-Watz, H. & Tärnvik, A. Duct ELISA for detection of bacteria in fluid samples. *J. Microbiol. Methods* **5** (1), 41–47 (1986) .
- [20] Peters, R. P. H., van Agtmael, M. A., Danner, S. A., Savelkoul, P. H. M. & Vandenbroucke-Grauls, C. M. J. E. New developments in the diagnosis of bloodstream infections. *Lancet Infect. Dis.* **4** (12), 751–760 (2004) .
- [21] Klouche, M. & Schröder, U. Rapid methods for diagnosis of bloodstream infections. *Clin. Chem. Lab. Med.* **46** (7), 888–908 (2008) .
- [22] Murray, P. R. & Masur, H. Current approaches to the diagnosis of bacterial and fungal bloodstream infections in the intensive care unit. *Crit. Care Med.* **40** (12), 3277–3282 (2012) .
- [23] Decuyper, S. *et al.* Diagnosis of bacterial bloodstream infections: A 16S metagenomics approach. *PLoS Negl. Trop. Dis.* **10** (2), e0004470 (2016) .
- [24] Kneipp, K., Kneipp, H. & Kneipp, J. Surface-Enhanced raman scattering in local optical fields of silver and gold NanoaggregatesFrom Single-Molecule raman spectroscopy to ultrasensitive probing in live cells. *Acc. Chem. Res.* **39** (7), 443–450 (2006) .

- [25] Ou, Y.-C. *et al.* Multimodal multiplexed immunoimaging with nanostars to detect multiple immunomarkers and monitor response to immunotherapies. *ACS Nano* **14** (1), 651–663 (2020) .
- [26] Atkins, C. G., Buckley, K., Blades, M. W. & Turner, R. F. B. Raman spectroscopy of blood and blood components. *Appl. Spectrosc.* **71** (5), 767–793 (2017) .
- [27] Indrasekara, A. S. D. S. *et al.* Gold nanostar substrates for SERS-based chemical sensing in the femtomolar regime. *Nanoscale* **6** (15), 8891–8899 (2014) .
- [28] Jackson, J. B. & Halas, N. J. Surface-enhanced raman scattering on tunable plasmonic nanoparticle substrates. *Proc. Natl. Acad. Sci. U. S. A.* **101** (52), 17930–17935 (2004) .
- [29] Alonso-González, P. *et al.* Resolving the electromagnetic mechanism of surface-enhanced light scattering at single hot spots. *Nat. Commun.* **3** (1), 1–7 (2012) .
- [30] De Silva Indrasekara, A. S. & Fabris, L. SERS-based approaches toward genetic profiling. *Bioanalysis* **7** (2), 263–278 (2015) .
- [31] Guarrotxena, N., Liu, B., Fabris, L. & Bazan, G. C. Antitags: nanostructured tools for developing SERS-based ELISA analogs. *Adv. Mater.* **22** (44), 4954–4958 (2010) .
- [32] Fabris, L., Schierhorn, M., Moskovits, M. & Bazan, G. C. Aptatag-based multiplexed assay for protein detection by surface-enhanced raman spectroscopy. *Small* **6** (14), 1550–1557 (2010) .
- [33] Talamona, F. *et al.* Stable and scalable SERS tags conjugated with neutravidin for the detection of fibroblast activation protein (FAP) in primary fibroblasts. *Nanotechnology* **32** (29) (2021) .
- [34] Er, E. *et al.* Metal Nanoparticles/MoS<sub>2</sub> Surface-Enhanced raman Scattering-Based sandwich immunoassay for  $\alpha$ -Fetoprotein detection. *ACS Appl. Mater. Interfaces* **13** (7), 8823–8831 (2021) .
- [35] Krug, J. T., Wang, G. D., Emory, S. R. & Nie, S. Efficient raman enhancement and intermittent light emission observed in single gold nanocrystals. *J. Am. Chem. Soc.* **121** (39), 9208–9214 (1999) .
- [36] Xie, W. *et al.* Nuclear targeted nanoprobe for single living cell detection by Surface-Enhanced raman scattering. *Bioconj. Chem.* **20** (4), 768–773 (2009) .

- [37] Nie, S. & Emory, S. R. Probing single molecules and single nanoparticles by Surface-Enhanced raman scattering. *Science* **275** (5303), 1102–1106 (1997) .
- [38] Hadimioglu, B. *et al.* IEEE (ed.) *Acoustic ink printing*. (ed.IEEE) *IEEE 1992 Ultrasonics Symposium Proceedings*, 929–935 vol.2 (1992).
- [39] Elrod, S. A. *et al.* Nozzleless droplet formation with focused acoustic beams. *J. Appl. Phys.* **65** (9), 3441–3447 (1989) .
- [40] Hadimioglu, B., Elrod, S. & Sprague, R. Yuhas, D. & Schneider, S. (eds) *Acoustic ink printing: an application of ultrasonics for photographic quality printing at high speed*. (eds Yuhas, D. & Schneider, S.) *2001 IEEE Ultrasonics Symposium. Proceedings. An International Symposium (Cat. No.01CH37263)*, Vol. 1, 627–635 vol.1 (2001).
- [41] Shields, C. W., 4th, Reyes, C. D. & López, G. P. Microfluidic cell sorting: a review of the advances in the separation of cells from debulking to rare cell isolation. *Lab Chip* **15** (5), 1230–1249 (2015) .
- [42] Micciché, C. *et al.* Inkjet printing ag nanoparticles for SERS hot spots. *Anal. Methods* **10** (26), 3215–3223 (2018) .
- [43] Talbot, E. L., Berson, A., Brown, P. S. & Bain, C. D. Evaporation of picoliter droplets on surfaces with a range of wettabilities and thermal conductivities. *Phys. Rev. E* **85** (6), 061604 (2012) .
- [44] Tadesse, L. F. *et al.* Plasmonic and electrostatic interactions enable uniformly enhanced liquid bacterial Surface-Enhanced raman scattering (SERS). *Nano Lett.* **20** (10), 7655–7661 (2020) .
- [45] Berry, V., Gole, A., Kundu, S., Murphy, C. J. & Saraf, R. F. Deposition of CTAB-Terminated nanorods on bacteria to form highly conducting hybrid systems. *J. Am. Chem. Soc.* **127** (50), 17600–17601 (2005) .
- [46] Fernandes, H. P., Cesar, C. L. & Barjas-Castro, M. d. L. Electrical properties of the red blood cell membrane and immunohematological investigation. *Rev. Bras. Hematol. Hemoter.* **33** (4), 297–301 (2011) .
- [47] Hayashi, K. *et al.* Red blood Cell-Shaped microparticles with a red blood cell membrane demonstrate prolonged circulation time in blood. *ACS Biomater Sci Eng* **4** (8), 2729–2732 (2018) .
- [48] Sreeprasad, T. S. & Pradeep, T. Reversible assembly and disassembly of gold nanorods induced by EDTA and its application in SERS tuning. *Langmuir* **27** (7), 3381–3390 (2011) .

- [49] Su, L., Zhang, P., Zheng, D.-W., Wang, Y.-J.-Q. & Zhong, R.-G. Rapid detection of escherichia coli and salmonella typhimurium by surface-enhanced raman scattering. *Optoelectronics Letters* **11**, 157–160 (2015) .
- [50] Moghtader, F., Tomak, A., Zareie, H. M. & Piskin, E. Bacterial detection using bacteriophages and gold nanorods by following time-dependent changes in raman spectral signals. *Artif. Cells Nanomed. Biotechnol.* **46** (sup2), 122–130 (2018) .
- [51] Witkowska, E., Niciński, K., Korsak, D., Szymborski, T. & Kamińska, A. Sources of variability in SERS spectra of bacteria: comprehensive analysis of interactions between selected bacteria and plasmonic nanostructures. *Anal. Bioanal. Chem.* **411** (10), 2001–2017 (2019) .
- [52] Wang, Y., Lee, K. & Irudayaraj, J. Silver nanosphere SERS probes for sensitive identification of pathogens. *J. Phys. Chem. C* **114** (39), 16122–16128 (2010) .
- [53] Sivanesan, A. *et al.* Nanostructured silver–gold bimetallic SERS substrates for selective identification of bacteria in human blood. *Analyst* **139** (5), 1037–1043 (2014) .
- [54] Choi, J., Lee, J. & Jung, J. H. Fully integrated optofluidic SERS platform for real-time and continuous characterization of airborne microorganisms **169**, 112611 (2020) .
- [55] Zhou, H. *et al.* SERS detection of bacteria in water by in situ coating with ag nanoparticles. *Anal. Chem.* **86** (3), 1525–1533 (2014) .
- [56] Drescher, D., Büchner, T., McNaughton, D. & Kneipp, J. SERS reveals the specific interaction of silver and gold nanoparticles with hemoglobin and red blood cell components. *Phys. Chem. Chem. Phys.* **15** (15), 5364–5373 (2013) .
- [57] Premasiri, W. R., Lee, J. C. & Ziegler, L. D. Surface-enhanced raman scattering of whole human blood, blood plasma, and red blood cells: cellular processes and bioanalytical sensing. *J. Phys. Chem. B* **116** (31), 9376–9386 (2012) .
- [58] Reokrungruang, P., Chatnuntawech, I., Dharakul, T. & Bamrungsap, S. A simple paper-based surface enhanced raman scattering (SERS) platform and magnetic separation for cancer screening. *Sens. Actuators B Chem.* **285**, 462–469 (2019) .
- [59] Paccotti, N. *et al.* Label-Free SERS discrimination and in situ analysis of life cycle in escherichia coli and staphylococcus epidermidis. *Biosensors*

8 (4) (2018) .

- [60] Zhang, S., Li, Z. & Wei, Q. Smartphone-based cytometric biosensors for point-of-care cellular diagnostics. *Nanotechnology and Precision Engineering* **3** (1), 32–42 (2020) .
- [61] Arya, S. K., Lim, B. & Rahman, A. R. A. Enrichment, detection and clinical significance of circulating tumor cells. *Lab Chip* **13** (11), 1995–2027 (2013) .
- [62] Jeffrey, S. S. & Toner, M. Liquid biopsy: a perspective for probing blood for cancer. *Lab Chip* **19** (4), 548–549 (2019) .
- [63] Glynn, M. T., Kinahan, D. J. & Ducrée, J. CD4 counting technologies for HIV therapy monitoring in resource-poor settings—state-of-the-art and emerging microtechnologies. *Lab Chip* **13** (14), 2731–2748 (2013) .
- [64] Stöckel, S. *et al.* Raman spectroscopic identification of mycobacterium tuberculosis. *J. Biophotonics* **10** (5), 727–734 (2017) .
- [65] Khan, S. *et al.* Analysis of tuberculosis disease through raman spectroscopy and machine learning. *Photodiagnosis Photodyn. Ther.* **24**, 286–291 (2018) .
- [66] Kaewseekhao, B. *et al.* Diagnosis of active tuberculosis and latent tuberculosis infection based on raman spectroscopy and surface-enhanced raman spectroscopy. *Tuberculosis* **121**, 101916 (2020) .
- [67] Ye, X., Zheng, C., Chen, J., Gao, Y. & Murray, C. B. Using binary surfactant mixtures to simultaneously improve the dimensional tunability and monodispersity in the seeded growth of gold nanorods. *Nano Lett.* **13** (2), 765–771 (2013) .
- [68] Radziuk, D. & Moehwald, H. Prospects for plasmonic hot spots in single molecule SERS towards the chemical imaging of live cells. *Phys. Chem. Chem. Phys.* **17** (33), 21072–21093 (2015) .
- [69] Kuang, M. *et al.* Inkjet printing patterned photonic crystal domes for wide viewing-angle displays by controlling the sliding three phase contact line. *Adv. Opt. Mater.* **2** (1), 34–38 (2014) .
- [70] Yang, Q. *et al.* Highly reproducible SERS arrays directly written by inkjet printing. *Nanoscale* **7** (2), 421–425 (2014) .
- [71] Zhang, H. *et al.* Spherical nanoparticle arrays with tunable nanogaps and their hydrophobicity enhanced rapid SERS detection by localized concentration of droplet evaporation. *Adv. Mater. Interfaces* **2** (9), 1500031

(2015) .

- [72] Gao, Y., You, T., Yang, N., Zhang, C. & Yin, P. Superhydrophobic 3D forest-like ag microball/nanodendrite hierarchical structure as SERS sensor for rapid droplets detection. *Adv. Mater. Interfaces* **6** (8), 1801966 (2019) .
- [73] Shin, S. *et al.* A droplet-based high-throughput SERS platform on a droplet-guiding-track-engraved superhydrophobic substrate. *Small* **13** (7), 1602865 (2017) .
- [74] Panda, S. S., Ames, D. P. & Panigrahi, S. Application of vegetation indices for agricultural crop yield prediction using neural network techniques. *Remote Sensing* **2**, 673–696 (2010) .
- [75] Rodrigues, J. *et al.* Exploring photoacoustic spectroscopy-based machine learning together with metabolomics to assess breast tumor progression in a xenograft model ex vivo. *Lab. Invest.* **101** (7), 952–965 (2021) .
- [76] Ehrentreich, F. & Sümmchen, L. Spike removal and denoising of raman spectra by wavelet transform methods. *Anal. Chem.* **73** (17), 4364–4373 (2001) .
- [77] Ramos, P. M. & Ruisánchez, I. Noise and background removal in raman spectra of ancient pigments using wavelet transform. *J. Raman Spectrosc.* **36** (9), 848–856 (2005) .
- [78] Harris, C. R. *et al.* Array programming with NumPy. *Nature* **585** (7825), 357–362 (2020) .
- [79] Pedregosa, F. *et al.* Scikit-learn: Machine learning in python. *J. Mach. Learn. Res.* **12** (85), 2825–2830 (2011) .
- [80] Alsmeyer, F. & Marquardt, W. Automatic generation of peak-shaped models. *Appl. Spectrosc.* **58** (8), 986–994 (2004) .
- [81] Sundius, T. Computer fitting of voigt profiles to raman lines. *J. Raman Spectrosc.* **1** (5), 471–488 (1973) .

# Supplementary Information: Detecting pathogenic bacteria in blood with combined acoustic bioprinting, Raman spectroscopy, and machine learning

Fareeha Safir<sup>1\*</sup>, Nhat Vu<sup>2</sup>, Loza F. Tadesse<sup>3</sup>, Kamyar Firouzi<sup>4</sup>, Niaz Banaei<sup>5,6,7</sup>, Stefanie S. Jeffrey<sup>8</sup>, Amr. A. E. Saleh<sup>9,10\*</sup>, Butrus (Pierre) Khuri-Yakub<sup>4,11</sup> and Jennifer A. Dionne<sup>10,12\*</sup>

<sup>1\*</sup>Department of Mechanical Engineering, Stanford University, Stanford, 94305, CA, United States.

<sup>2</sup>Pumpkinseed Technologies, Inc., Palo Alto, 94306, CA, United States.

<sup>3</sup>Department of Bioengineering, Stanford University School of Medicine and School of Engineering, Stanford, 94305, CA, United States.

Present Address: Department of Electrical Engineering and Computer Science, University of California, Berkeley, Berkeley, 94720, CA, United States.

<sup>4</sup>E. L. Ginzton Laboratory, Stanford University, Stanford, 94305, CA, United States.

<sup>5</sup>Department of Pathology, Stanford University School of Medicine, Stanford, 94305, CA, United States.

<sup>6</sup>Clinical Microbiology Laboratory, Stanford Health Care, Palo Alto, 94304, CA, United States.

<sup>7</sup>Department of Infectious Diseases and Geographic Medicine, Stanford University School of Medicine, Stanford, 94305, CA, United States.

<sup>8</sup>Department of Surgery, Stanford University School of Medicine, Stanford, 94305, CA, United States.

<sup>9</sup>Department of Engineering Mathematics and Physics, Cairo University, Cairo, 12613, Egypt.

<sup>10</sup>Department of Materials Science and Engineering, Stanford University, Stanford, 94305, CA, United States.

<sup>11</sup>Department of Electrical Engineering, Stanford University, Stanford, 94305, CA, United States.

<sup>12</sup>Department of Radiology, Molecular Imaging Program at Stanford (MIPS), Stanford University School of Medicine, Stanford, 94305, CA, United States.

\*To whom correspondence should be addressed; E-mail: [fsafir@stanford.edu](mailto:fsafir@stanford.edu); [aessawi@eng.cu.edu.eg](mailto:aessawi@eng.cu.edu.eg); [jdionne@stanford.edu](mailto:jdionne@stanford.edu);

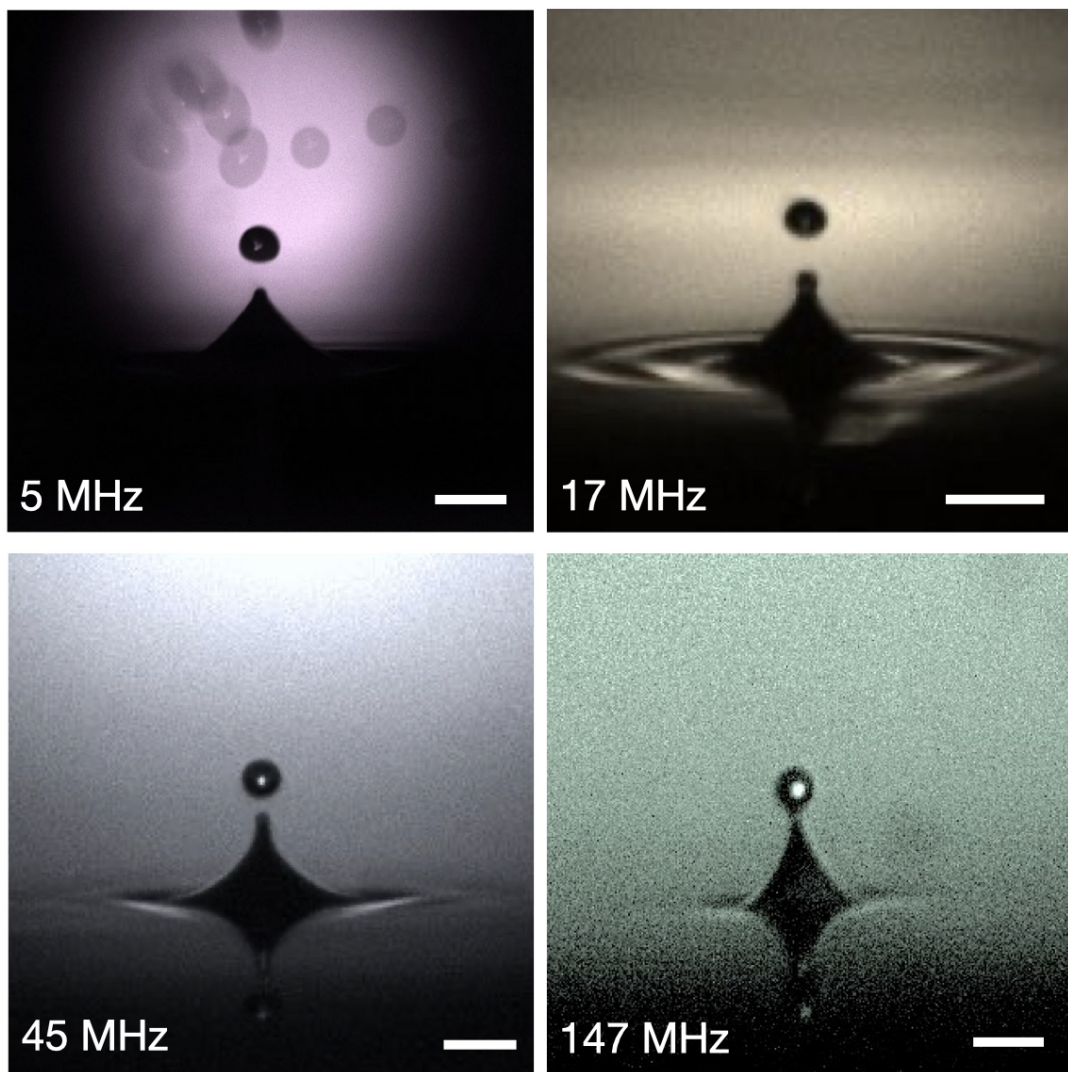
## Supplementary Note 1: Gold nanorods for SERS applications

SERS is a phenomenon that provides Raman intensity signal enhancements of on average of  $10^5$ - $10^6$ , with localized hotspots providing enhancements of  $10^8$ - $10^{10}$  [1–3]. Commonly, SERS utilizes metallic substrates that, through their plasmonic and chemical effects (such as charge transfer ability), enhance both the electric field from the incident light and the Raman scattered light from the sample, resulting in fourth order enhancement in the local electric field  $|E|^4$  [4–10]. SERS typically relies on metallic substrates to provide these enhancements. For biosensing applications, it is important for these substrates to provide large enhancements while being tunable, reproducible, stable, and inexpensive [11]. As such, colloidal nanoparticles have gained traction as one of the primary forms of metallic SERS substrates [8, 12–16]. In the realm of biosensing, gold and silver nanorods have been the primary metals used for SERS substrate synthesis due to their chemical stability and low toxicity [8, 11, 17–19]. Particularly ideal for biological sensing, nanoparticles with sharp tips, such as nanocubes, nanostars [20], nanopyramids, and nanorods, provide large Raman spectral enhancement factors, with nanorods providing the best balance of stability, reproducibility, tunability, cost, and enhancement [4, 21]. Furthermore, due to their pervasiveness, gold nanorod (GNR) synthesis and properties are well documented allowing for reproducibility and easy tunability of optical properties through choice of particle size and shape [12, 22–26]. Finally, advances in SERS substrates such as nanoparticle-on-mirror (NPoM) constructs [4, 27], nanogaps and nanoholes [11, 28, 29], graphene based nanodot arrays [30], and core-shell alloys [31–33] are paving the way for future Raman-based biosensing applications.

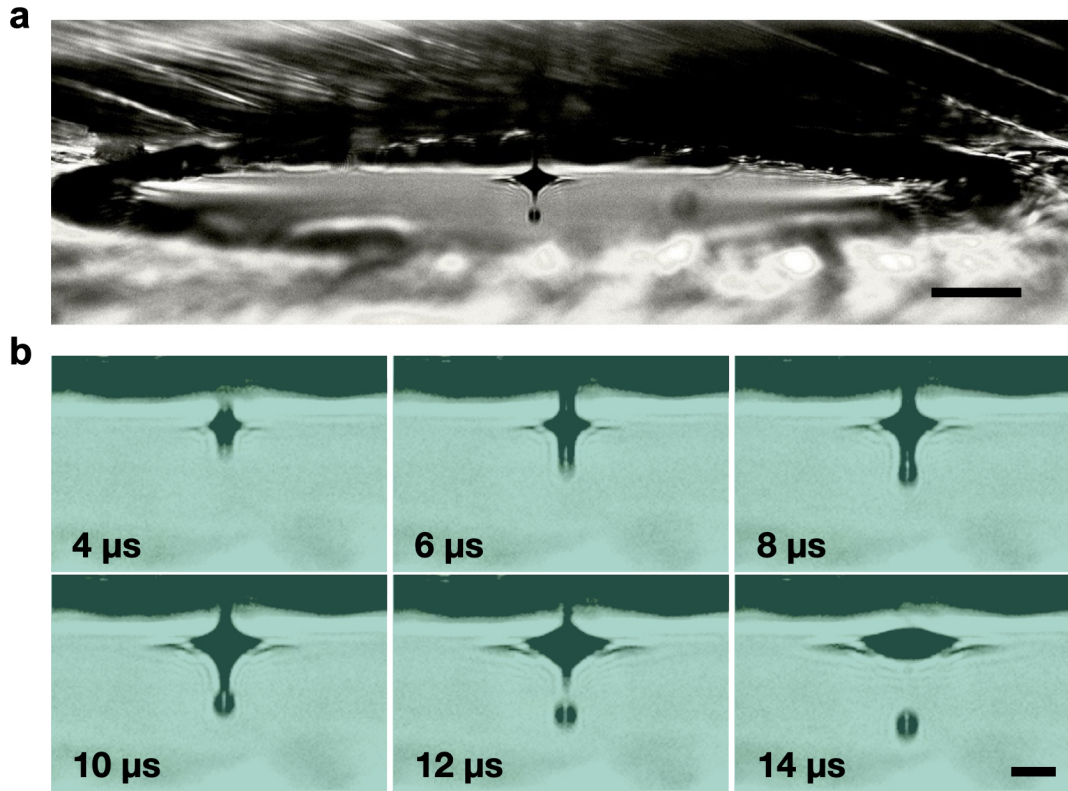
## Supplementary Note 2: Acoustic printing for handling biological samples

Acoustic printing works by using ultrasonic waves to eject a droplet from a free surface of fluid. A radio frequency (RF) burst signal is used to excite a transducer at its resonant frequency, generating ultrasonic waves that exert force on the fluid surface [34, 35]. When the focus of the transducer is aligned with the liquid-air interface and the intensity of the acoustic field is high enough, the generated radiation pressure will overcome the surface tension and the sound wave gives rise to a mound of fluid from the surface [35, 36]. If the energy of the incident wave exceeds the threshold energy, a droplet breaks free from the fluid surface at a velocity of a few meters per second due to the Rayleigh-Taylor instability [34, 37]. The droplet diameter has been shown to closely match the diffraction-limited focal width at the liquid-air interface, and as such, the droplet diameter is inversely proportional to the frequency of the transducer, with 5 MHz and 300 MHz ultrasonic waves generating droplet diameters of 300  $\mu\text{m}$  and 5  $\mu\text{m}$ , respectively [35]. (see Fig. 1a). ADE droplet

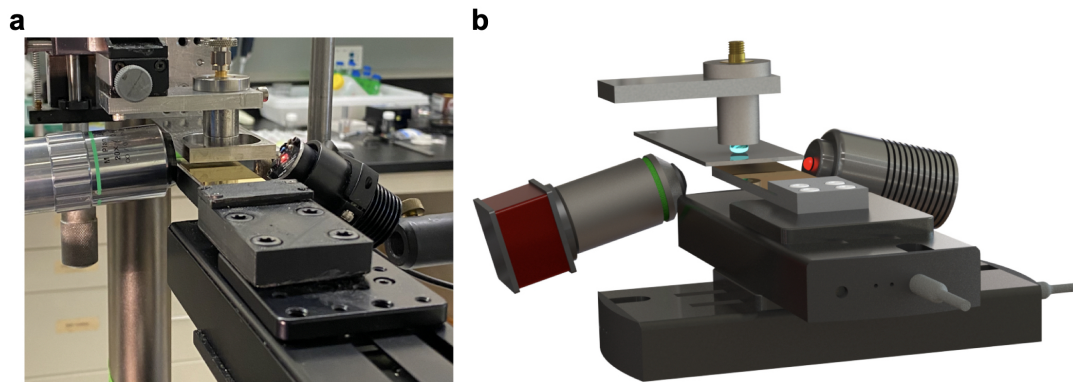
ejection has been well characterized and has great tunability for handling a variety of biological samples [38]. Furthermore, the focused ultrasonic waves completely control the size, speed, and directionality of the ejected droplet and allow for ADE from an open liquid surface. Given that the dimensions of this open liquid surface are much larger than the diameter of the focal spot size, ADE is considered a nozzle-less technology [39]. This holds true for our downwards setup utilizing an ejection plate, given that our focal spot size is  $\sim 2$  orders of magnitude smaller than the 1 mm diameter hole [34, 35]. As a nozzle-less technology, ADE has unparalleled advantage in biological sample handling as compared with other commercial piezo or thermal inkjet printers that rely on physical flow focusing. In particular, ADE eliminates system clogging and compromised cell viability or biomarker structure due to shear forces generated by nozzles. Additionally, ADE relies on ultrasonic waves to generate droplets, as such, the transducer never has to contact the ejection medium, but rather can propagate through a matched coupling medium, eg. through the bottom of an acoustically “transparent” multiwell plate, with minimal loss of acoustic energy, mitigating risks of sample contamination and loss of sterility [39]. ADE has also gained traction for versatility in setup and ability for high-throughput droplet generation. For a single acoustic ejector, the limiting factor for droplet ejection rate is the dissipation of capillary waves propagating radially outwards on the fluid surface after ejection [34, 40]. Advances in ADE have led to improvements in fabrication methods of the focusing lenses and ejector arrays including: spherical lenses in silicon, spherical PZT shells, and fresnel acoustic lenses [34, 41]. These advancements have lead to the development of high-throughput ejector arrays greater than 1000 print heads and ejection rates of 25 kHz, allowing for ejection of a 10 mL of fluid in under an hour [41]. Furthermore, these advances have expanded the utility of ADE for biological samples handling to include cellular acoustic printing [38, 42, 43], biological crystallography [44–46], high-throughput screening (HTS) of biological agents [47], and for sample preparation in MALDI [48], highlighting the vast potential for biological analysis with ADE.



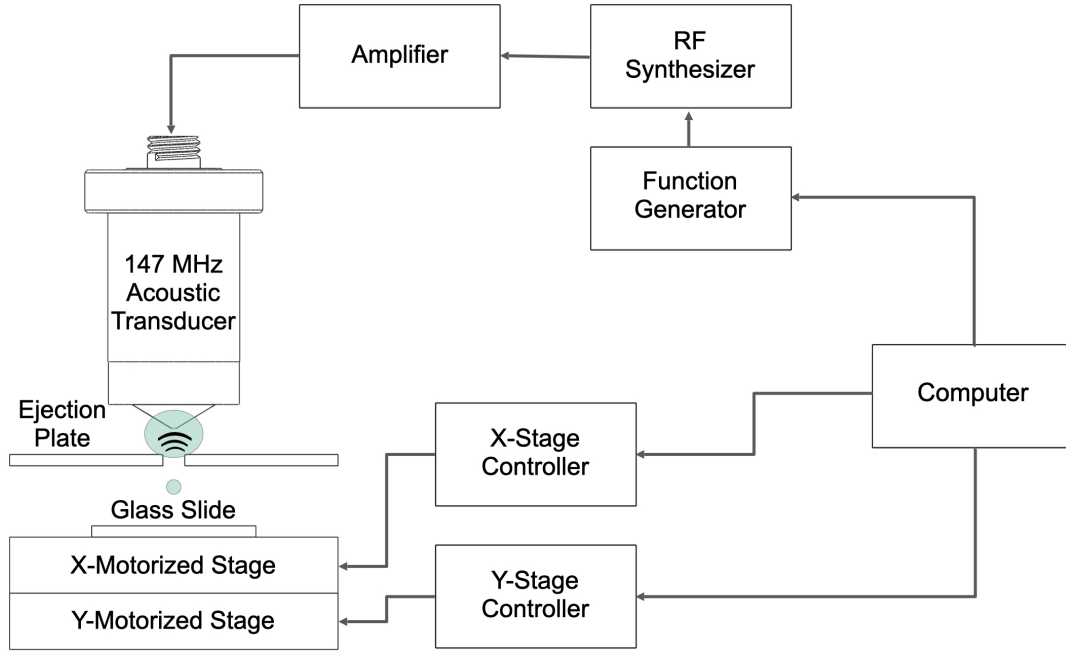
**Supplementary Fig. 1** Photographs of droplets printed with a range of acoustic frequencies. Droplets were printed with 4.8 MHz, 17 MHz, 44.75 MHz, and 147 MHz and had droplet diameters of 300  $\mu\text{m}$ , 84  $\mu\text{m}$ , 44  $\mu\text{m}$ , and 15  $\mu\text{m}$  respectively, highlighting the tunability of acoustic droplet ejection. Scale bars are 500  $\mu\text{m}$ , 200  $\mu\text{m}$ , 100  $\mu\text{m}$ , and 25  $\mu\text{m}$  respectively.



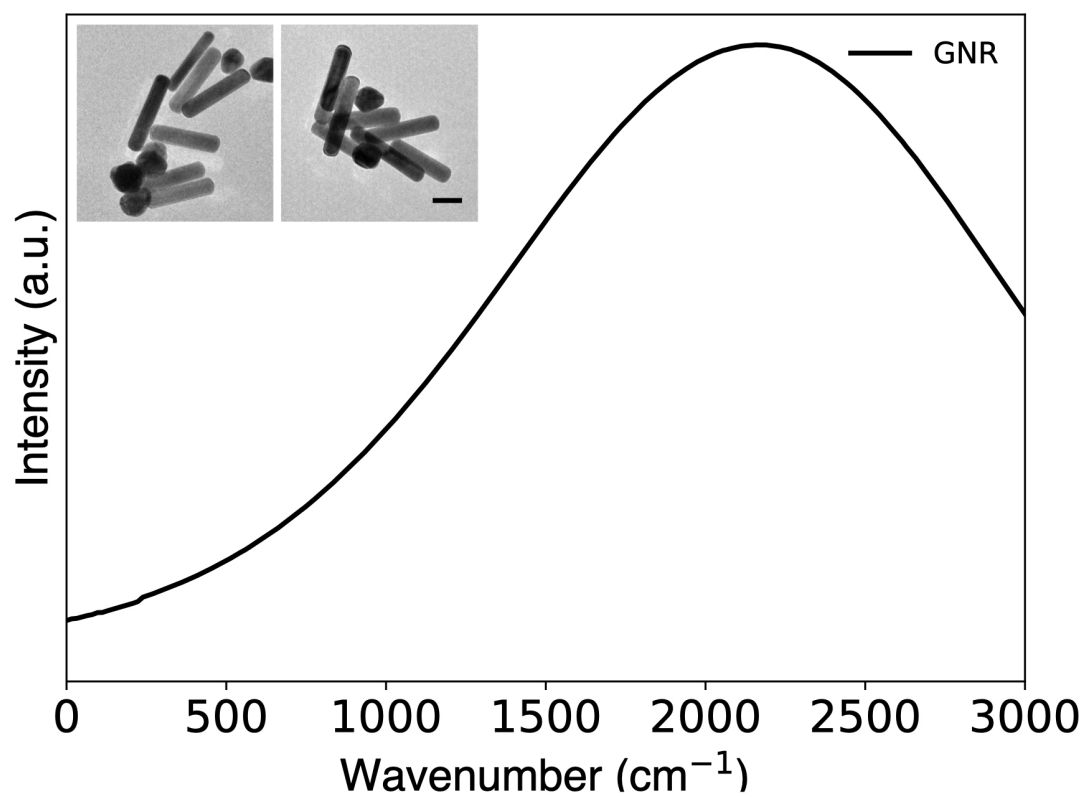
**Supplementary Fig. 2** **a**, Stroboscopic photograph showing a droplet being ejected downwards through the 1 mm hole on our ejection plate. Droplet was ejected from a pool of deionized water using a transducer operating at 147 MHz, Photo was taken with a 12  $\mu\text{s}$  phase delay after the burst was triggered. Scale bar is 100  $\mu\text{m}$ . **b**, Stroboscopic images of the time evolution of downward droplet ejection through the 1 mm hole at an acoustic frequency of 147 MHz. Droplet shown here is 15  $\mu\text{m}$  in diameter and  $\sim 2$  pL in volume. Droplet was ejected with 0.096  $\mu\text{J}$  of energy with a pulse width of 5.5  $\mu\text{s}$ , and was ejected downwards at  $\sim 3.5$  m/s. Scale bar is 100  $\mu\text{m}$ . All images were captured with an image exposure time of 40 ms and a droplet ejection rate of 1 kHz. As such, each frame is composed of 40 droplet ejections.



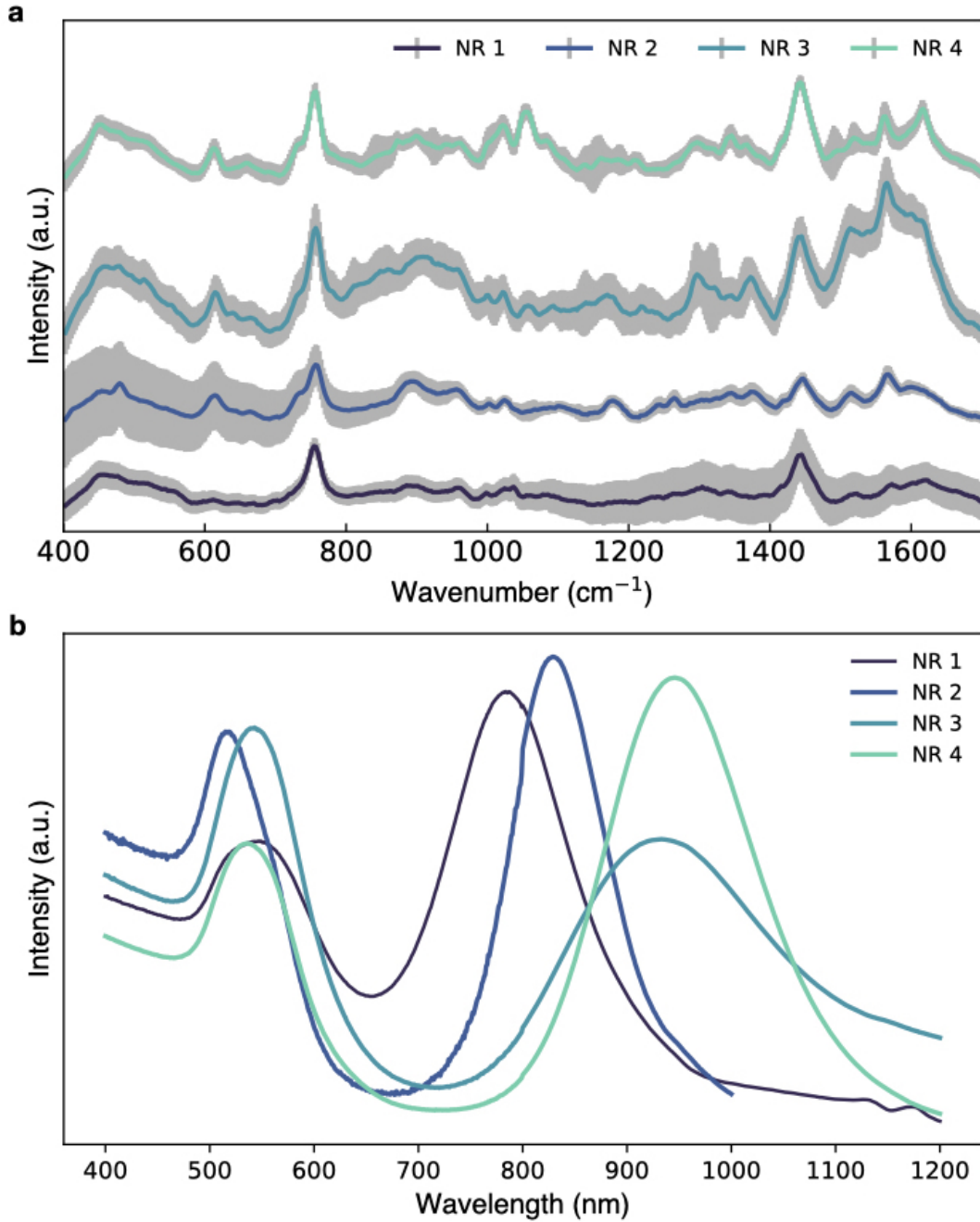
**Supplementary Fig. 3** Photo **a**, and rendering **b**, showing acoustic printing setup, including camera with 20x objective, baseplate with 1 mm diameter hole, strobing LED, gold-coated glass slide mounted onto a motorized XY stage, acoustic transducer, and printing fluid (teal).



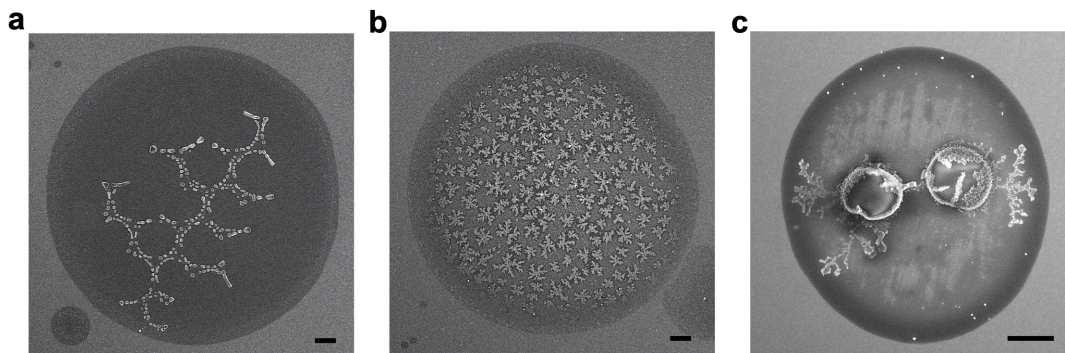
**Supplementary Fig. 4** Schematic showing the acoustic droplet ejection setup. The printing fluid (teal) rests between the focused acoustic transducer and the ejection plate with the 1 mm hole, held in place through surface tension. The droplets are ejected downwards onto a gold-coated glass slide mounted onto a motorized XY stage (stacked single axis stages). The burst signals to the transducer are generated from a function generator, routed through an RF synthesizer, and finally through a power amplifier before reaching the transducer. Ejection and movement of the mounted slide are controlled synchronously using MATLAB code.



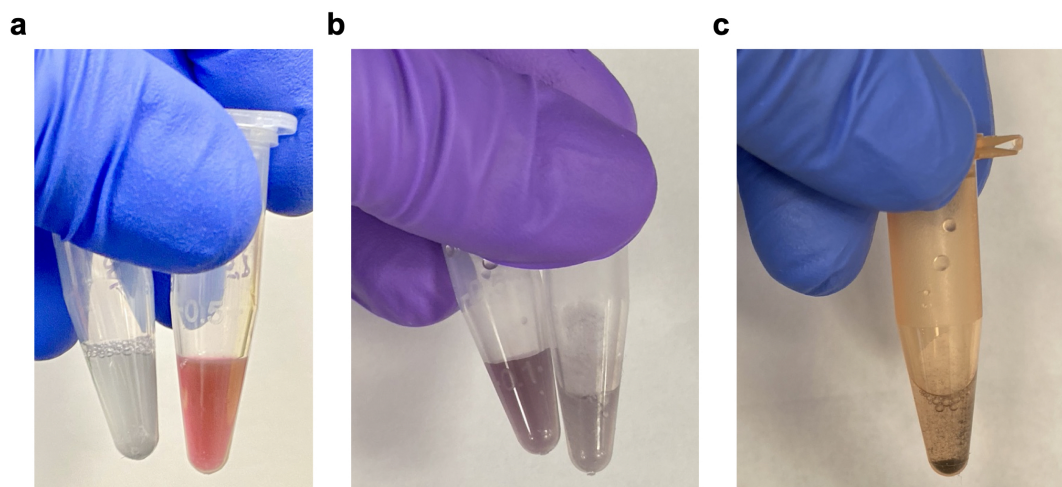
**Supplementary Fig. 5** Absorption spectra of GNRs used for Raman spectroscopy. Inset shows TEM of GNRs. Scale bar is 50 nm.



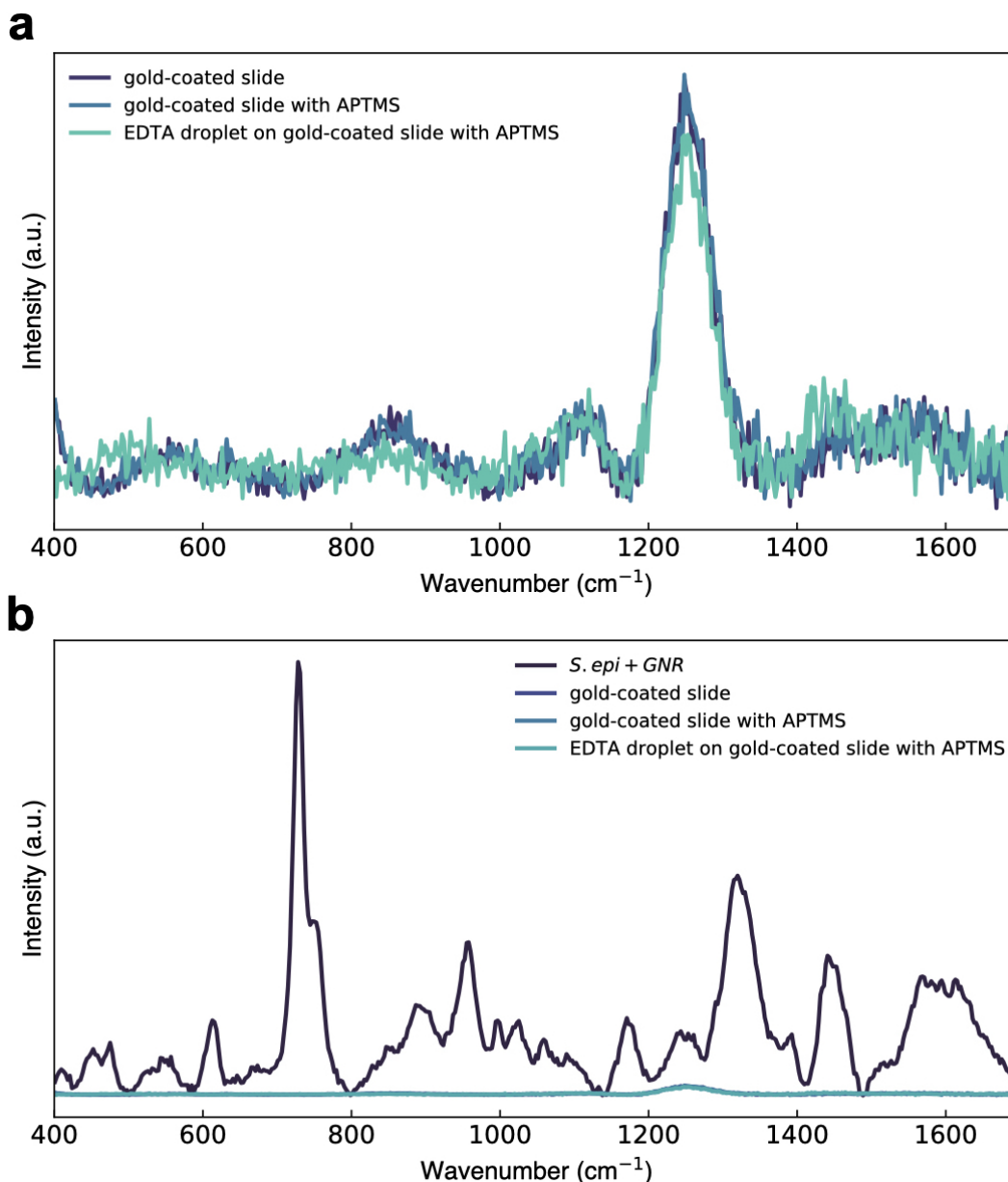
**Supplementary Fig. 6** Bacterial interrogation across multiple nanorod syntheses and resonance frequencies. We synthesized 4 different batches of GNRs and evaluated bacterial droplets with each batch. **a**, UV-Vis measurements of the 4 rods showing a range of resonance frequencies between 770 nm and 960 nm. Our chosen nanorods are those listed as NR4. **b**, Average spectral intensities and standard deviations collected from droplets printed with each of our four GNR batches mixed with *S. epi* bacteria diluted to a final concentration of  $1 \times 10^9$  cells/mL in a 1:9 mixture v/v of Invitrogen UltraPure 0.5M EDTA, Invitrogen 15575020, and Mili-Q purified water onto a silanized, gold-coated glass slide. Spectra were collected with a 10x objective lens with a 0.25 NA and  $\sim 10.6$  mW power. Each droplet was interrogated with a time study of 5 time points, with each exposure lasting 15 seconds. 10 droplets were analyzed from each GNR batch for a total of 50 data points across each group. The data shows the primary *S. epi* peaks around 731 and  $1317 \text{ cm}^{-1}$ , with varying max intensities, highlighting both the robustness of our system for spectral collection as well as the potential for improvements through tuning of GNR aspect ratio.



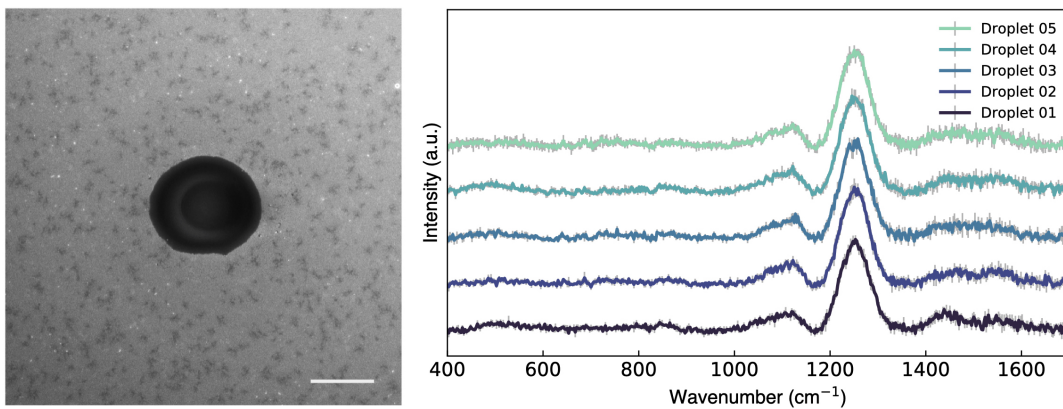
**Supplementary Fig. 7** Crystallization of saline upon drying in acoustically printed droplets printed at 147 MHz. Droplets **a**, and **b**, were printed from a 10% v:v phosphate buffered saline (PBS) solution. Droplet **c**, was printed with a mixture of mouse RBCs suspended in 10% v:v PBS solution. Scale bars are 10, 10, 5  $\mu\text{m}$ , respectively.



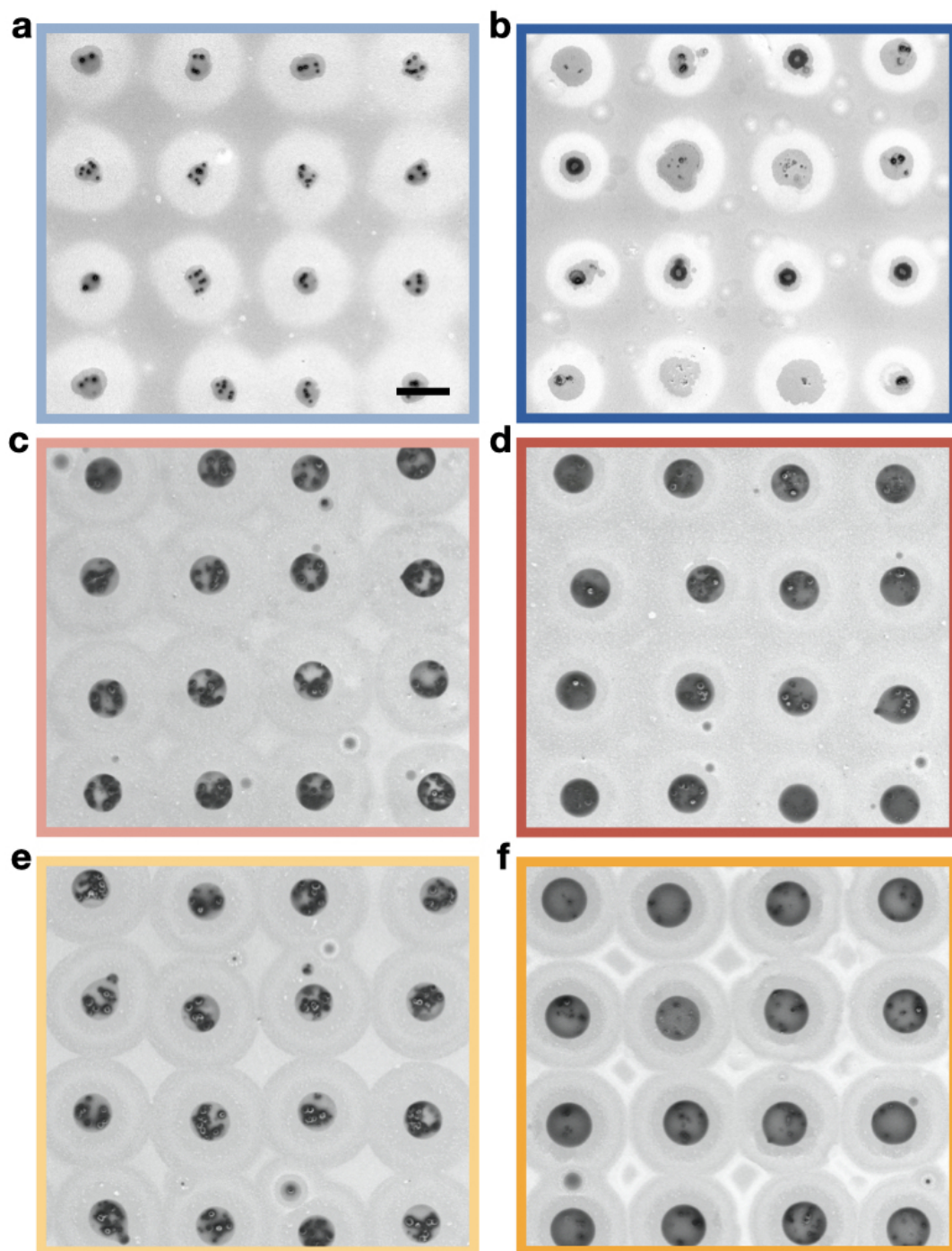
**Supplementary Fig. 8** Studying the effect of the EDTA on the nanorod dispersion in fluid. **a**, Photograph showing colorimetric comparison of gold nanorods (GNR) in (left) a 1:9 mixture of Invitrogen UltraPure 0.5 M EDTA, Invitrogen 155750, and Milli-Q purified water and (right) Milli-Q purified water only. **b**, Photograph showing colorimetric comparison of GNRs mixed with *S. epi* bacteria at a concentration of  $1\text{e}9$  cells/mL. The image shows the gold nanorods and bacteria in (left) Milli-Q purified water only and (right) in a 1:9 ratio v/v of EDTA solution and Milli-Q purified water. **c**, Photograph showing the settling of solution of GNRs, *S. epi* at a concentration of  $1\text{e}9$  cells/mL, and a 1:9 ratio v/v of EDTA solution to Milli-Q purified water. Photograph was taken 5 min after the solution was mixed together. We note that these images highlight that, as expected, the EDTA appears to aggregate the GNRs into clusters. As the *S. epi* bacteria seem to cause clustering regardless of the presence of the EDTA due to their surface charge, the difference between the sample with and without the EDTA is less noticeable than in the samples of only GNRs.



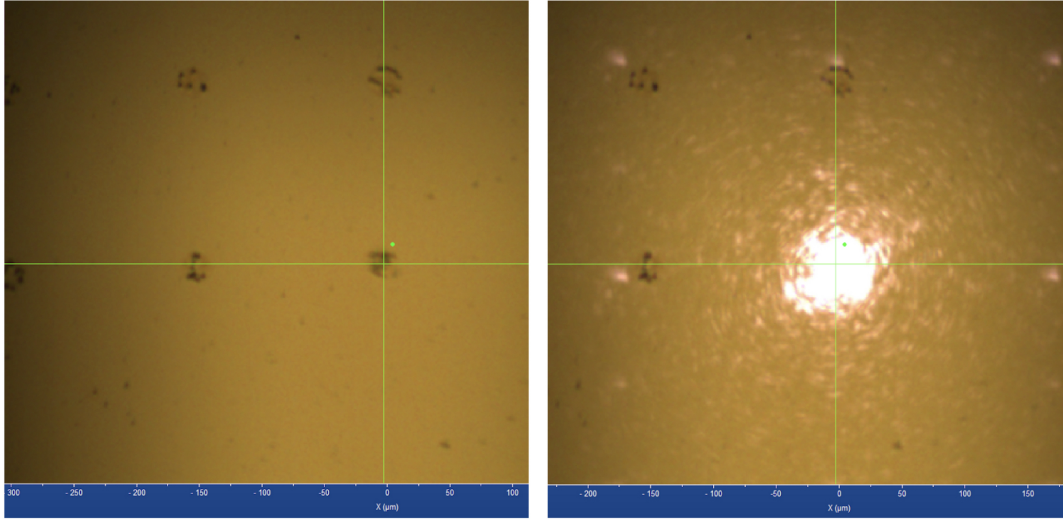
**Supplementary Fig. 9** Raman of background signals. **a**, Spectra were collected of a gold-coated glass slide, a gold-coated glass slide with an APTMS silane layer, and of a droplet printed onto a gold-coated glass slide with APTMS. Droplets were printed from Invitrogen UltraPure 0.5M EDTA, Invitrogen 15575020, mixed in a 1:9 ratio v/v with Mili-Q purified water. The spectra show that most of the background signal comes from the gold substrate with little additional background from our APTMS deposition and the additional EDTA used in our cell solutions. **b**, Identical spectra to that shown in **a** overlaid with a spectrum taken of *S. epi* bacteria and GNRs suspended in EDTA solution at a concentration of  $1\text{e}9$  cells/mL. The plot highlights that the spectral signal intensity from our bacteria is much higher than that of the background. All spectra were collected with a 10x objective lens with a 0.25 NA and  $\sim 10.6$  mW power for 15 s.



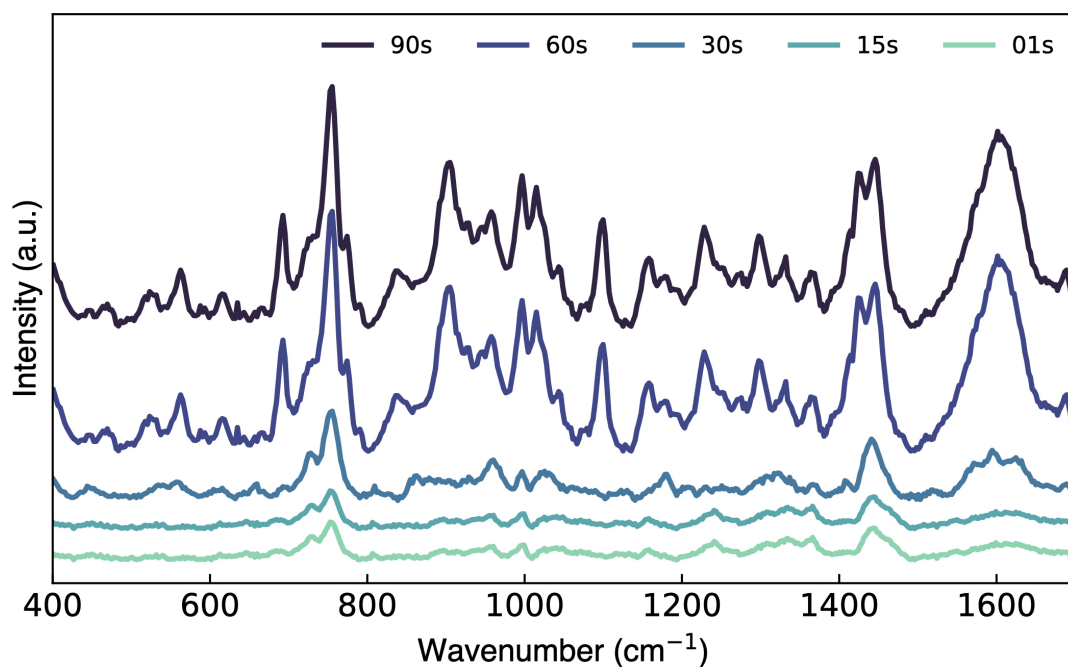
**Supplementary Fig. 10** Droplets were printed from cellular dilution mixture without any cells. Droplets were printed from Invitrogen UltraPure 0.5 M EDTA, Invitrogen 15575020, mixed in a 1:9 ratio v/v with Mili-Q purified water onto a silanized, gold-coated glass slide. Spectra were collected with a 10x objective lens with a 0.25 NA and  $\sim 10.6$  mW power for 15 s. The SEM clearly shows minimal spread of the EDTA solution onto the gold-coated slide. The spectra show minimal, and consistent background signals from the EDTA solution. Scale bar is 5  $\mu\text{m}$ .



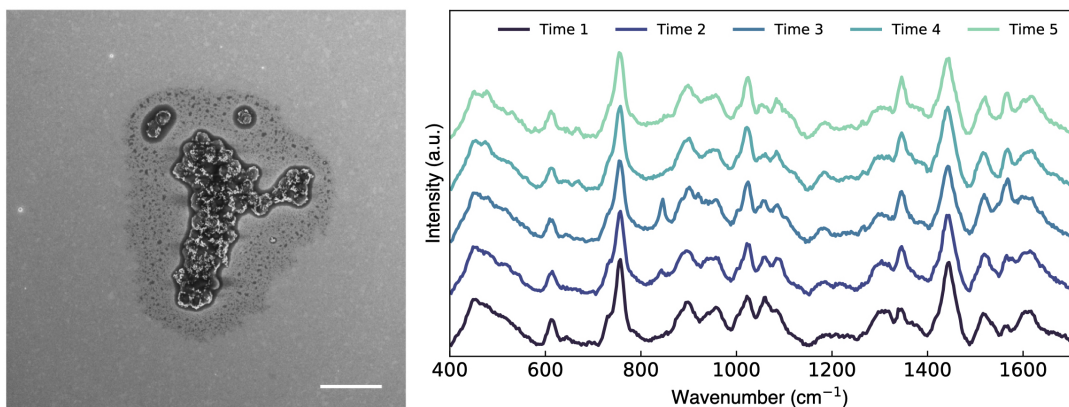
**Supplementary Fig. 11** SEMs of grids printed with cell and GNR mixtures. SEMs show 16 droplets imaged out of a grid of over 400 droplets. Mixtures were printed from cells with and without GNRs diluted in a 1:9 mixture of EDTA solution and Milli-Q water to a final concentration of  $1 \times 10^9$  cells/mL. All grids were acoustically printed using a transducer operating at 147 MHz with a  $5.5 \mu\text{s}$  pulse width burst signal. SEMs show **a**, *S. epi* **b**, *S. epi* mixed with GNRs both ejected with  $0.096 \mu\text{J}$  of acoustic energy and **c**, mouse RBCs **d**, mouse RBCs mixed with GNRs **e**, 1:1 mixture of *S. epi* and mouse RBCs **f**, 1:1 mixture of *S. epi* and mouse RBCs with GNRs all printed with  $0.139 \mu\text{J}$  of acoustic energy. The lighter and darker circles in each photo highlight the outer edge of the droplet as well as the smaller volume formed from the dried EDTA mixture containing our cells and GNRs in the center of the droplet. Scale bar is  $50 \mu\text{m}$ .



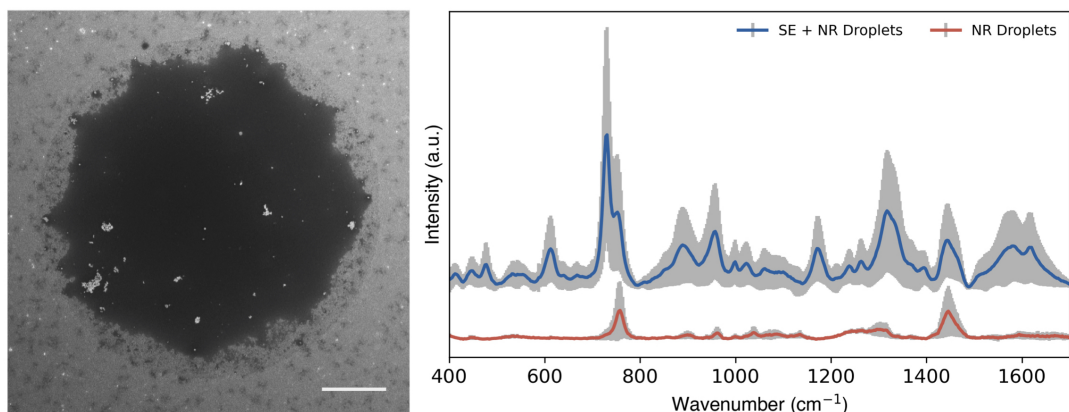
**Supplementary Fig. 12** Raman focal spot size. Images show screen shots from Horiba XploRA Raman confocal microscope UI. The image on the left shows an array of droplets printed onto an APTMS silanized, gold-coated slide. Droplets were printed from a solution of gold nanorods and *S.epi* bacteria at a concentration of  $1e9$  cells/mL, suspended in a solution of Invitrogen UltraPure 0.5 M EDTA, Invitrogen 15575020, mixed in a 1:9 ratio v/v with Milli-Q water. The image on the right shows the same array of droplets, with the 10x objective with the 785 nm laser turned on, operating at 25% laser power or  $\sim 10.6$  mW of power. This laser spot size is  $\sim 2$   $\mu\text{m}$ .



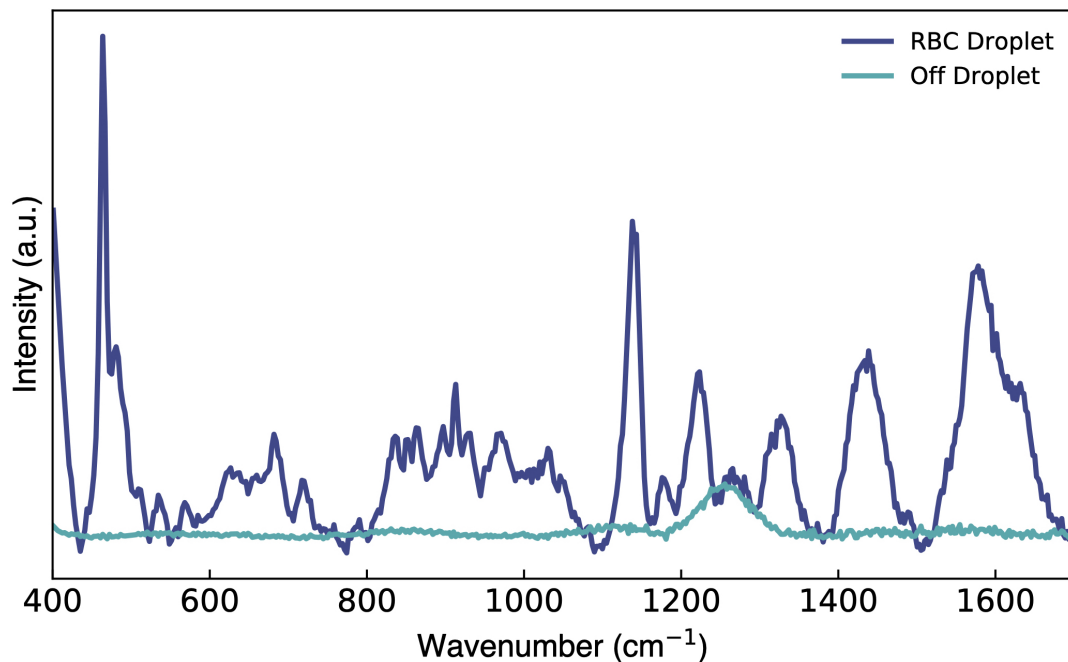
**Supplementary Fig. 13** Intensity study of single droplet with *S. epi* bacteria and GNRs taken at 1, 15, 30, 60, and 90 seconds. Droplets were printed from a mixture of GNRs and *S. epi* bacteria at a final concentration of 1e9 cells/mL diluted in a 1:9 v/v of Invitrogen UltraPure 0.5 M EDTA, Invitrogen 15575020, and Mili-Q purified water onto a silanized, gold-coated glass slide. Spectra were collected with a 10x objective lens with a 0.25 NA and ~10.6 mW power. The spectra show increasing signal intensity and signal complexity with each longer exposure time. This highlights that our time selection of 15 s is well below the time at which our sample gets damaged by the laser power. This analysis guided our choice of a 15 s acquisition time to balance gathering clear, distinct spectra with choosing a fast enough acquisition time to show potential for clinical translation.



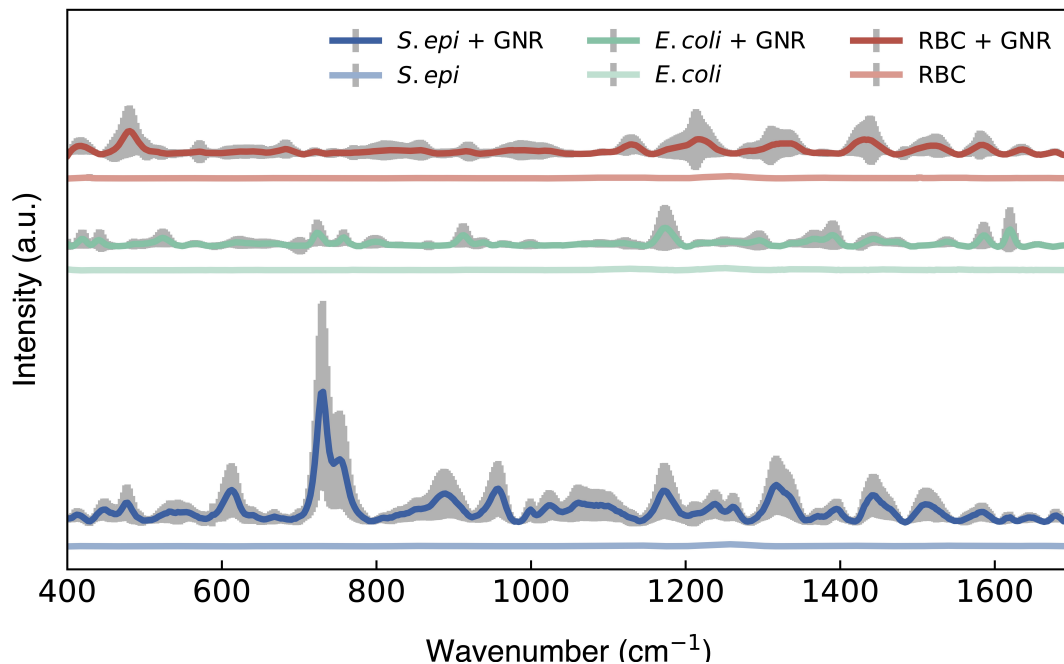
**Supplementary Fig. 14** Time study of single droplet with *S. epi* bacteria and GNRs across multiple time points. Droplets were printed from a mixture of GNRs and *S. epi* bacteria at a final concentration of  $1 \times 10^9$  cells/mL diluted in a 1:9 v/v of Invitrogen UltraPure 0.5 M EDTA, Invitrogen 15575020, and Mili-Q purified water onto a silanized, gold-coated glass slide. Spectra were collected with a 10x objective lens with a 0.25 NA and  $\sim 10.6$  mW power. Each spectrum was collected for 15 s in a time series lasting a total of 75 seconds. The SEM clearly shows a cluster of bacteria coated in GNRs. The spectra show minimal variation over the 75 second duration, showing that our acquisition time of 15 seconds does not damage the cells. Scale bar is  $5 \mu\text{m}$ .



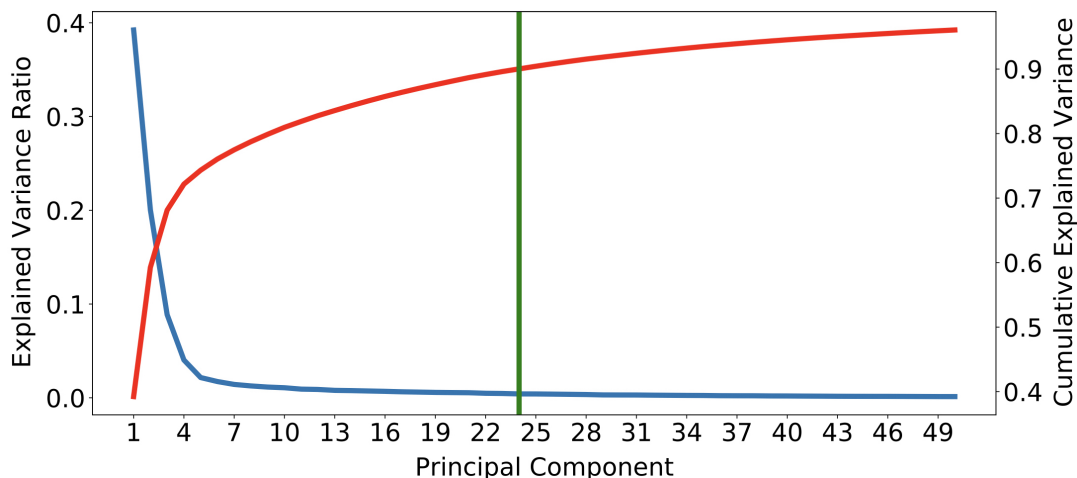
**Supplementary Fig. 15** Background signal from gold nanorods (GNR). Droplets were printed from a sample containing GNRs suspended without any cells in a 1:9 v/v mixture of Invitrogen UltraPure 0.5 M EDTA, Invitrogen 15575020, and Mili-Q purified water onto a silanized, gold-coated glass slide. Spectra were collected of each droplet with a 10x objective lens with a 0.25 NA and  $\sim 10.6$  mW power for 15 s. The SEM shows a droplet containing a few clusters of GNRs clearly distinguishable, highlighting both the presence of the GNRs and the absence of a coffee-ring of nanorods. The plot shows the mean and standard deviation of 100 droplets printed from a sample of *S. epi* bacteria with GNRs in EDTA solution (in blue, identical to that from Fig. 3), and the mean and standard deviation of 20 droplets printed from the GNR solution without cells. The spectra show that while the GNRs have a background signal, hypothesized to be from any remaining CTAB present in the solution after rinsing the rods, the cells have a clearly distinguishable signal separate from that of the GNRs, similar to our baseline *S. epi* spectra. Scale bar is  $5 \mu\text{m}$ .



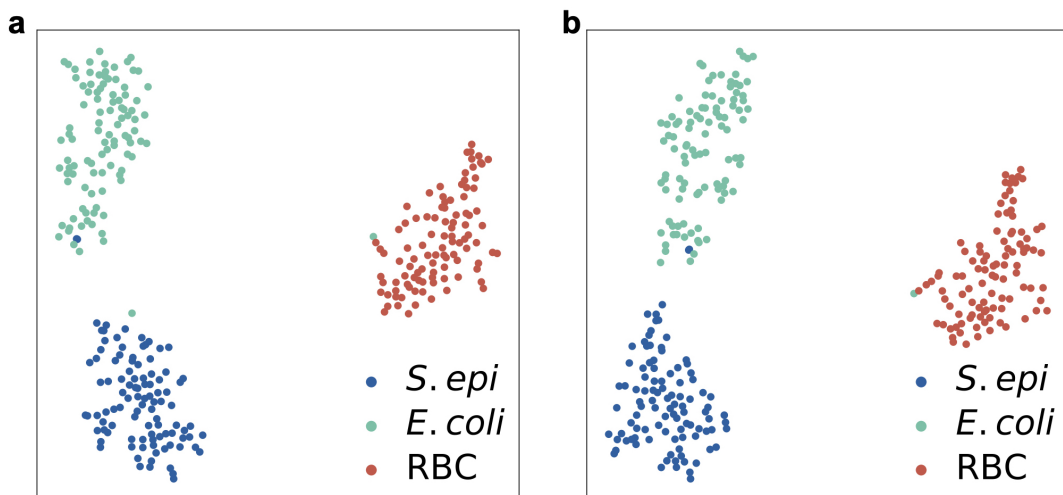
**Supplementary Fig. 16** Spectra were collected from a sample of droplets printed from GNRs mixed with mouse RBCs at a final concentration of  $1 \times 10^9$  cells/mL diluted in a 1:9 ratio v/v of Invitrogen UltraPure 0.5 M EDTA, Invitrogen 15575020, and Mili-Q purified water onto a silanized, gold-coated glass slide. Spectra were collected with a 10x objective lens with a 0.25 NA and  $\sim 10.6$  mW power for 15 s. The first spectra is taken while the focal spot is centered on the droplet while the other is taken when on the silanized gold substrate to the side of the droplet highlighting that our signal is coming directly from the droplet and not from any background material on the slide.



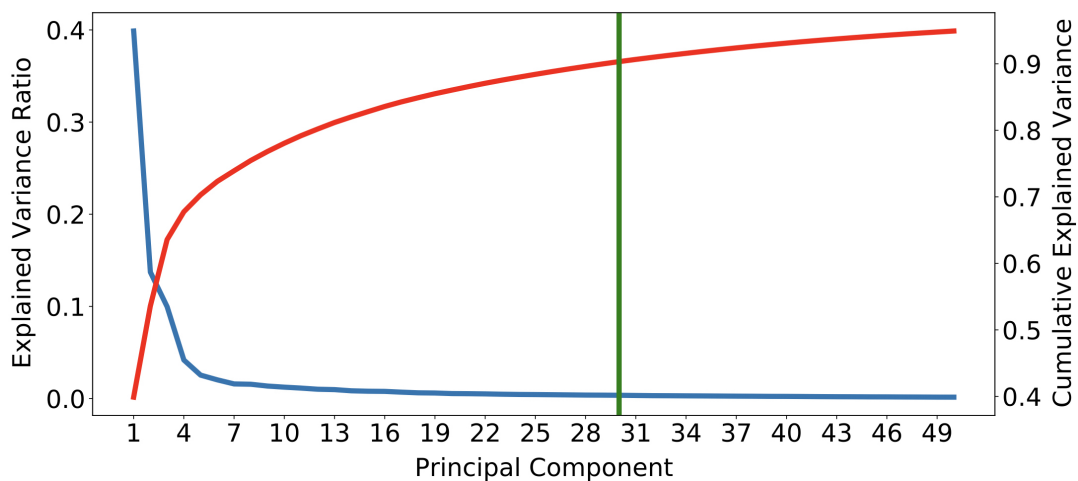
**Supplementary Fig. 17** Plot showing the mean and standard deviation of SERS spectra taken from droplets printed from three cell lines (*S. epi*, *E. coli*, and RBCs) with and without GNRs. Spectra were collected from 100 and 15 droplets, respectively. The plots highlight both the enhancements generated with the presence of GNRs as well as the variations in peak spectra intensity due to the variations in surface charge density on each cell line and subsequently the cells' varying attraction to the positive surface charge of the GNRs, resulting from the CTAB surfactant on their surface [49].



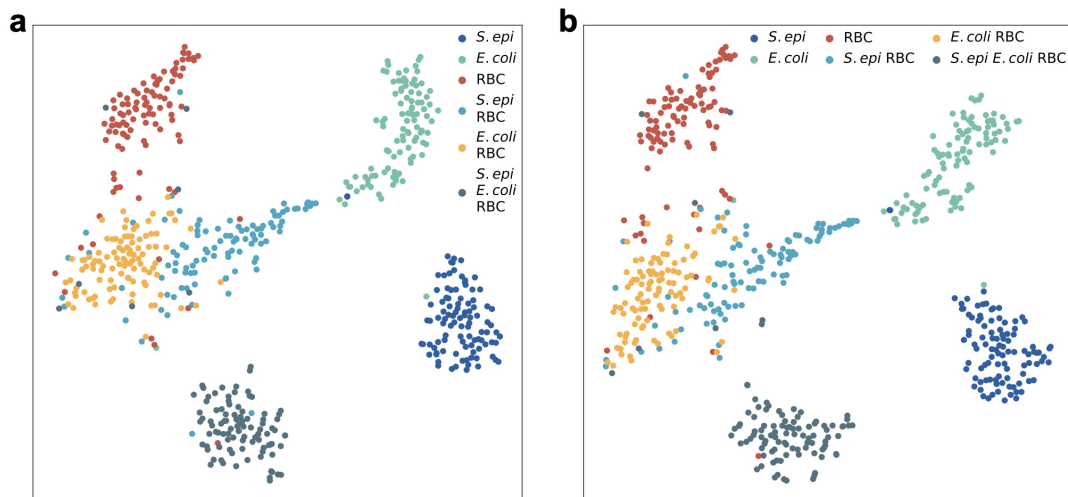
**Supplementary Fig. 18** Plot of the percentage of variance attributed to each principal component and the cumulative explained variance over 50 components. The green line indicates the number of PCA components necessary to capture 90% of all explained variance in our samples. For all 300 spectra from our single cell-line droplets, we demonstrate that we can account for at least 90% of all variance with 24 components generated from all 508 wavenumber features in our spectra.



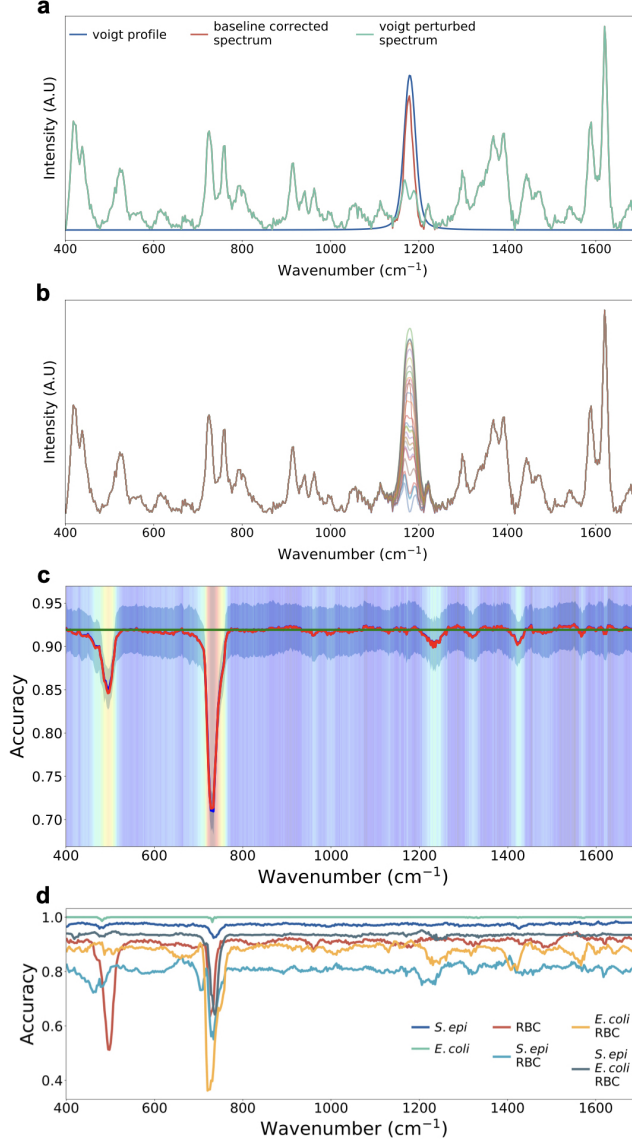
**Supplementary Fig. 19** Plots showing a 2-component, t-distributed stochastic neighbor embedding projection (t-SNE) with perplexity = 10 across our 3 single cell-line classes. Data is plotted **a**, with data inclusive of all wavenumber features and **b**, after performing a 24-component PCA for dimensionality reduction. Plots show relative clustering of our classes and minimal variation to clustering after dimensionality reduction.



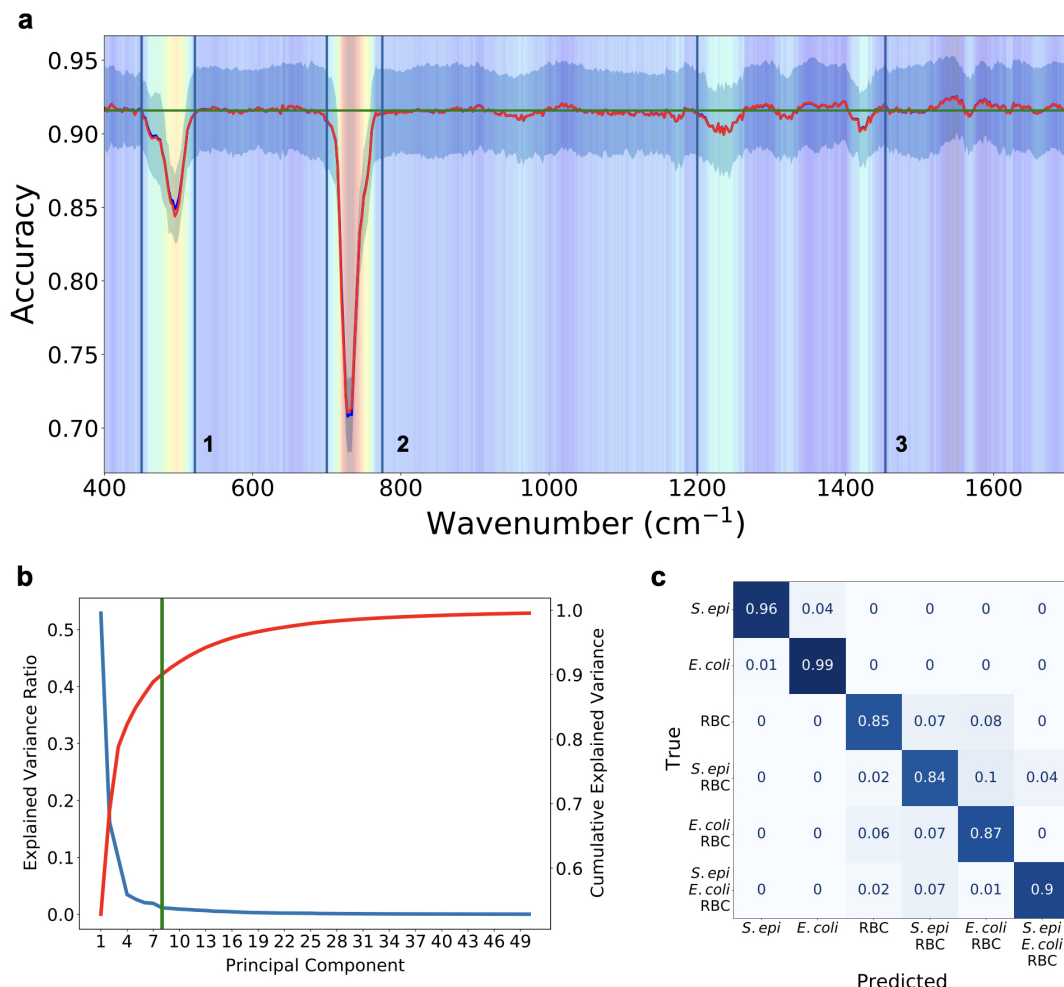
**Supplementary Fig. 20** Plot of the percentage of variance attributed to each principal component and the cumulative explained variance over 50 components. The green line indicates the number of PCA components necessary to capture 90% of all explained variance in our samples. For all 600 spectra from our 3 single cell-line droplet classes and our 3 cell mixture classes, we demonstrate that we can account for at least 90% of all variance with 30 components generated from all 508 wavenumber features in our spectra.



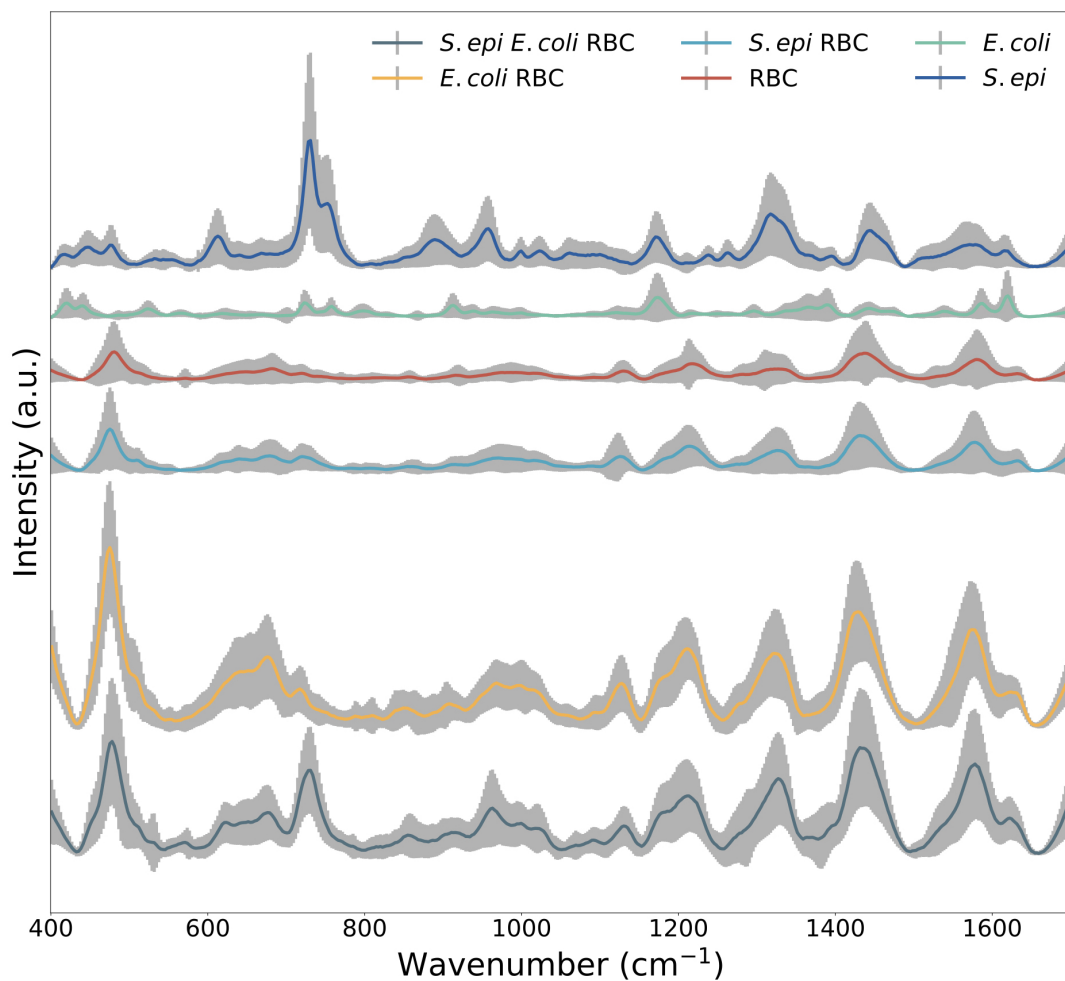
**Supplementary Fig. 21** Plots showing a 2-component, t-distributed stochastic neighbor embedding projection (t-SNE) with perplexity = 10 across all 6 of our classes. Data is plotted **a**, with data inclusive of all wavenumber features and **b**, after performing a 30-component PCA for dimensionality reduction. Plots show relative clustering of our classes and minimal variation to clustering after dimensionality reduction.



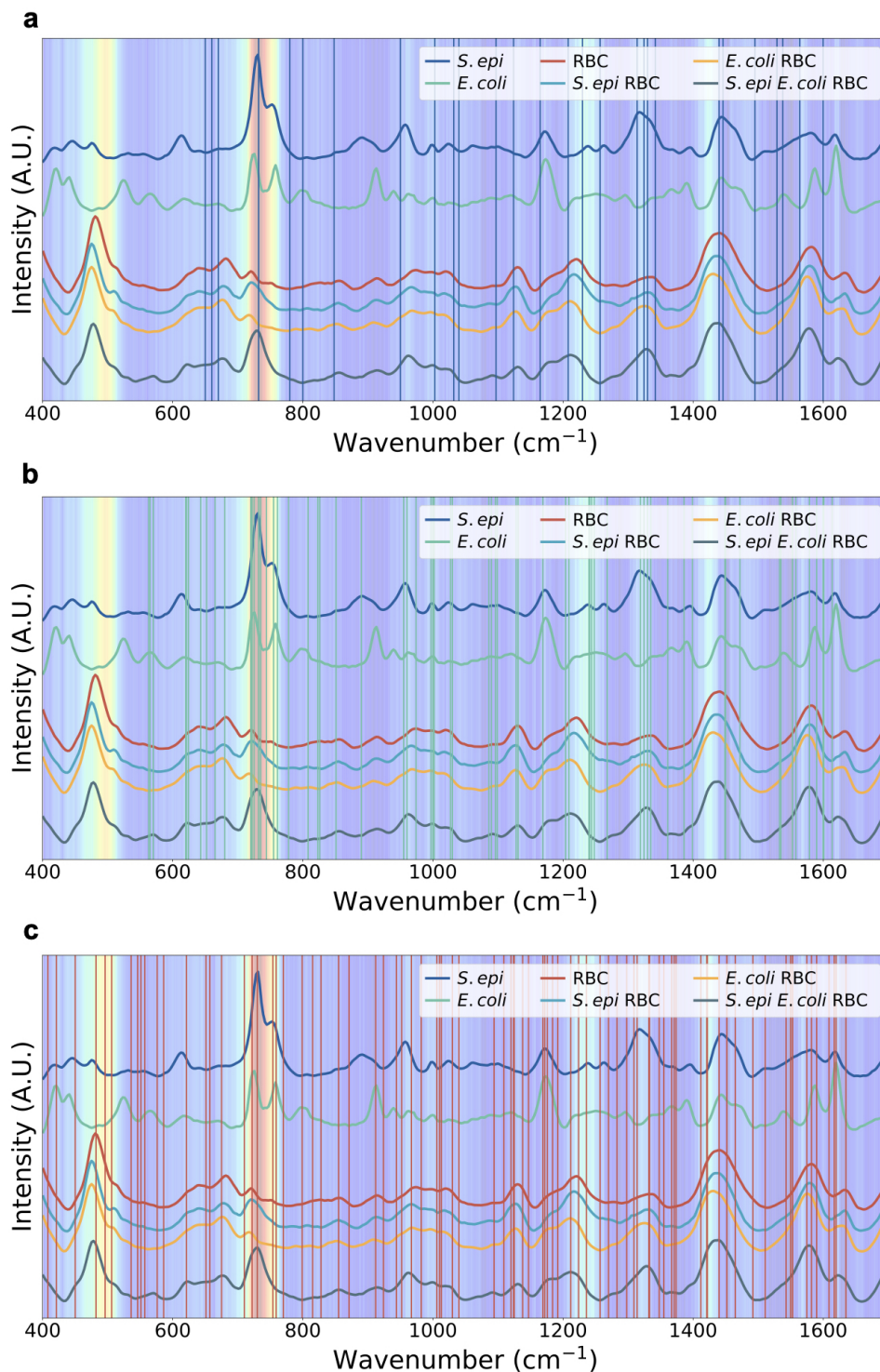
**Supplementary Fig. 22** Feature Validation. We perform feature validation on our spectra to determine which wavenumbers and spectral bands are most important for our classifier. We take our 600 spectra across all 6 cellular classes and split the samples using a stratified shuffle split into an 80:20 train/test split. For each spectrum in our training set, we iteratively perturb the spectrum at each wavenumber. After each perturbation, we calculate the classification accuracy and compare with our baseline accuracy. Every wavenumber of each spectrum in the test set is perturbed 5 times and all results are averaged for our final feature extraction. Spectra were perturbed with a normalized Voigt profile. Line width chosen to roughly match peak widths seen in our spectra. **a**, plot showing an example Voigt curve (blue), unperturbed example spectrum from our dataset (red), and perturbed spectrum (green). **b**, Voigt profile intensities were chosen through random sampling of all spectra in our training set. Plot shows an example of a spectrum from our sample set with 100 different perturbations. **c**, Heatmap highlighting feature validation performed to determine relative weight of spectral wavenumbers in our Random Forest classification. Heatmap is overlaid with a plot of mean and standard deviation of the perturbed classification accuracy (red) and f1 score (blue) calculated across all trials. Mean accuracy is plotted in green. Wavenumbers with lower accuracies are shown to be critical features, as random perturbations in these regions are highly correlated with decreases in classification accuracy. **d**, Plot of the mean classification accuracy broken down into accuracies across each of our cellular and mixture classes.



**Supplementary Fig. 23** Classification using spectral feature bands of interest evaluated across 600 spectra collected from single cell-line droplets of *S. epi*, *E. coli*, and mouse RBCs mixed with GNRs, and our 3 cell mixtures. **a**, Heatmap presented in Supplementary Fig. 22, highlighting feature importance calculations performed to determine relative weight of spectral wavenumbers in our random forest classification. Heatmap is overlaid with 3 bands representing key spectral bands used by our classifier. We further demonstrate that these bands are primarily responsible for our classification accuracies by preprocessing our spectra by removing spectral features outside these bands ( $420\text{--}522\text{ cm}^{-1}$ ,  $700\text{--}775\text{ cm}^{-1}$ ,  $1200\text{--}1454\text{ cm}^{-1}$ ). We then reduced the dimensionality of our remaining features using an 8-component PCA as previously reported. **b**, Plot of the percentage of variance attributed to each principal component and the cumulative explained variance over 50 components. The green line indicates the number of PCA components necessary to capture 90% of all explained variance in our samples. For this sample set taking only specific wavenumber bands from our spectra, we demonstrate that we can account for at least 90% of all variance with only 8 components generated from all 508 wavenumber features in our spectra. **c**, Finally, we use our previously described random forest classifier on our samples and perform a stratified K-fold cross validation of our classifier's performance across 10 splits. Results are plotted on a normalized confusion matrix. We show that we achieve  $\geq 81\%$  classification accuracy across all samples as compared with the  $\geq 87\%$  classification accuracy achieved when evaluating the entire spectra window from  $400\text{--}1700\text{ cm}^{-1}$ . These results further validate our feature recognition model. Furthermore, they pave the way for future development of low cost POC systems by demonstrating that the use of low-cost spectrometers with limited spectral windows may be possible for such diagnostic work.



**Supplementary Fig. 24** Plot showing the mean and standard deviation of SERS spectra taken from droplets printed from our 6 droplet classes: three single-cell line classes (*S. epi*, *E. coli*, and RBCs) and three mixture classes (equal mixtures of *S. epi* and RBCs, *E. coli* and RBCs, and *S. Epi*, *E. coli*, and RBCs) all diluted to a final concentration of 1e9 cells/mL of each cell type in our aqueous EDTA solution and mixed with GNRs. Spectra were collected from 100 droplets for each class.



**Supplementary Fig. 25** Heatmap highlighting feature extraction performed to determine relative weight of spectral wavenumbers in our random forest classification. Heatmap is overlaid with the mean SERS spectra of 100 measurements each, taken from single droplets printed from three cell lines (*S. epi*, *E. coli*, and RBCs) and three mixtures (*S. epi* and RBCs, *E. coli* and RBCs, and *S. epi*, *E. coli*, and RBCs) mixed with GNRs. Wavenumbers representative of biological peaks of dried and liquid SERS of **a**, *S. epi*, **b**, *E. coli*, and **c**, RBCs previously reported in the literature are plotted as vertical lines [49–60].

**Supplementary Table 1:** Tentative band assignments of the SERS spectra of *S. epi*, *E. coli*, RBCs as reported in literature.

Peak Pos. (cm <sup>-1</sup> )	Cell Type	Peak Assignment	Peak Pos. (cm <sup>-1</sup> )	Cell Type	Peak Assignment
408	RBC	$\delta(C_\beta C_a C_b)4 + \delta(C_\beta Me)$ [58]	1124	<i>S. epi</i>	$\nu(PO_2)$ [60]
421	RBC	$\delta(Fe-O-O)$ [57]		RBC	$\nu13$ or $\nu42$ [58]
450	RBC	Fe-O[57]	1125	RBC	Proteins: C-N stretch and C-C stretch[57]
482	RBC	$\gamma12$ [57]	1128	<i>E. coli</i>	Amide III, adenine, polyadenine, and DNA[56]
496	RBC	$\gamma12$ [58]	1138	RBC	$\nu(C_\beta\text{-Methyl})$ , $\nu5$ [57]
506	RBC	Fe-O, Proteins: S-S stretch[57]	1147	RBC	Proteins, lipids: C-N and C-C stretch[57]
536	RBC	$\gamma21$ , $\nu25$ , Proteins: S-S stretch, skeletal deform[57]	1165	<i>S. epi</i>	Tyr, Phe, amide III[60]
546	RBC	$\nu(Fe-O-O)$ [57]	1169	RBC	$\nu30$ [58]
551	RBC	$\nu49$ or $\nu(Fe-O-O)$ [58]		<i>E. coli</i>	12-methyltetraconic acid or 15-methylpalmitic acid or acetoacetate[50]
557	RBC	$\nu(Fe-O-O)$ [57]	1172	RBC	$\nu(\text{pyr half-ring})_{asym}$ , $\nu30$ [57]
565	<i>E. coli</i>	C-S-S-C[52]	1176	RBC	C-H bending, Tyr[59]
563	<i>E. coli</i>	Carbohydrates[56]	1184	RBC	Thr: CH <sub>3</sub> rocking[57]
570	<i>E. coli</i>	Carbohydrates[53]	1192	RBC	Thr: CH <sub>3</sub> rocking[57]
576	RBC	$\nu(Fe-O_2)$ [57]	1204	<i>E. coli</i>	Phe[60]
586	RBC	$\nu48$ [58]	1208	<i>S. epi</i>	Phe[60]
620	<i>E. coli</i>	Phe[52]	1209	<i>E. coli</i>	Aromatic amino acids in proteins[53]
621	<i>E. coli</i>	C-C twisting mode of Phe[60]	1212	RBC	$\delta(C_mH)$ , $\nu13$ or $\nu42$ [57]

Peak Pos. (cm <sup>-1</sup> )	Cell Type	Peak Assignment	Peak Pos. (cm <sup>-1</sup> )	Cell Type	Peak Assignment
	RBC	$\nu 12$ [58]	1224	RBC	$\delta(C_mH)$ [57] $\nu 13$ or $\nu 42$ [57, 58]
624	<i>E. coli</i>	Aromatic ring skeleton[56]	1230	<i>S. epi</i>	$\nu(PO_2^-)$ , amide III[60]
643	<i>E. coli</i>	Guanine ring breathing[60]	1235	<i>E. coli</i>	Vibration of N-H[51]
650	<i>S. epi</i>	Guanine ring breathing[60]	1236	RBC	Trp: ring[57]
651	RBC	Cys: C-S stretch[57]	1240	<i>E. coli</i>	Amide III[52]
652	<i>E. coli</i>	$\delta(COO^-)$ [56]	1241	<i>E. coli</i>	$\nu(PO_2^-)$ , amide III
657	RBC	$\delta(\text{pyr deform})_{sym}$ , $\nu 7$ [57]	1248	<i>E. coli</i>	CH <sub>2</sub> stretching[50]
659	<i>E. coli</i>	Guanine (C-S)[50]	1257	<i>S. epi</i>	Amide III[60]
660	<i>S. epi</i>	Guanine, thymine ring breathing[60]		RBC	Glu: CH <sub>2</sub> wag; proteins, lipids: amide III, $\delta(CH_2/CH_3)$ [57]
665	<i>E. coli</i>	NAG (N-acetylglucosamine)[60]	1268	<i>E. coli</i>	$\delta(CH_2)$ Amide III[56]
670	<i>S. epi</i>	NAG (N-acetylglucosamine)[60]	1270	RBCs	Proteins, lipids: amide III, $\delta(CH_2/CH_3)$ [57]
675	RBC	$\nu 7$ [58]	1283	RBC	$\delta(C_mH)$ , $\nu 21$ [57]
680	<i>E. coli</i>	Adenine[53]	1298	RBC	$\delta(C_mH)$ , $\nu 21$ [57]
710	RBC	$\nu 11$ [58]	1309	RBC	$\nu 21$ [58]
720	<i>E. coli</i>	Adenine in Flavin adenine dinucleotide (FAD) and Nicotinamide Adenine Dinucleotide (NAD)[52]	1314	<i>S. epi</i>	Guanine, CH <sub>2</sub> twist (lipids)[60]
722	<i>E. coli</i>	Adenine[50]		RBC	Phe, Glu, Ser, Met, His: CH <sub>2</sub> wag[57]
725	RBC	Amino acids: $\delta(COO^-)$ [57]	1319	<i>E. coli</i>	Guanine, CH <sub>2</sub> twist (lipids)[60]
	<i>E. coli</i>	Adenine ring breathing[60]	1324.5	<i>S. epi</i>	Protein and carboxylic stretches[55]

Peak Pos. (cm <sup>-1</sup> )	Cell Type	Peak Assignment	Peak Pos. (cm <sup>-1</sup> )	Cell Type	Peak Assignment
730	RBC	Amino acids: $\delta(\text{COO}^-)$ [57]		<i>E. coli</i>	Protein and carboxylic stretches[55]
731	<i>S. epi</i>	Adenine part of the flavin derivatives or glycosidic ring mode of polysaccharide[54]	1330	<i>S. epi</i>	Adenine part of the flavin derivatives or glycosidic ring mode of polysaccharides[54]
	<i>E. coli</i>	Adenine part of the flavin derivatives or glycosidic ring mode of polysaccharides[54]		<i>E. coli</i>	Adenine part of the flavin derivatives or glycosidic ring mode of polysaccharides[54] $\nu(\text{NH}_2)$ adenine, polyadenine, DNA[56] $\text{CH}_2/\text{CH}_3$ wagging mode in purine bases of nucleic acids[52] $\nu_{41}$ [58]
732.5	<i>S. epi</i>	purine ring-breathing modes[55]	1332	RBC	$\nu(\text{pyr half-ring})_{\text{sym}}$ , Proteins: $\delta(\text{CH})$ ; $\text{CH}_2$ , $\text{CH}_3$ wag[57]
735	<i>E. coli</i>	adenine, glycosidic ring mode[56]	1333	RBC	$\text{CH}_2$ deformation or Trp[50] Protein twisting ( $\text{CH}_2$ and $\text{CH}_3$ ), $\nu(\text{NH}_2)$ adenine[51, 60]
744	<i>E. coli</i>	$\text{B}_{1g}$ heme vibration (cytochrome c)[60]	1335	<i>E. coli</i>	Protein twisting ( $\text{CH}_2$ and $\text{CH}_3$ ), $\nu(\text{NH}_2)$ adenine[60]
754	RBC	$\nu_{15}$ [58] Porphyrin ring breathing[59]	1342	<i>S. epi</i>	Protein twisting ( $\text{CH}_2$ and $\text{CH}_3$ ), $\nu(\text{NH}_2)$ adenine[60]
755	<i>E. coli</i>	Trp ring breathing[60]	1348	RBC	Glu, Asp, Asn, Gln: $\text{CH}_2$ sciss, Ala, Leu, Val, Ile: $\text{CH}_3$ deform[57]
759	RBC	$\nu(\text{pyr breathe})$ , $\nu_{15}$ [57]	1355	<i>E. coli</i>	Ch deformation vibrations[51]

Peak Pos. (cm <sup>-1</sup> )	Cell Type	Peak Assignment	Peak Pos. (cm <sup>-1</sup> )	Cell Type	Peak Assignment
761	<i>E. coli</i>	Ring I deformation[53]		RBC	Glu, Asp, Asn, Gln: CH <sub>2</sub> sciss, Ala, Leu, Val, Ile: CH <sub>3</sub> deform[57]
770	RBC	Trp: indole sym. breathe[57]	1361	<i>E. coli</i>	=CH in plane (lipid) or amide III (protein)[53]
778	<i>E. coli</i>	DNA/RNA ring breathing (cytosine/thymine)[60]	1367	RBC	Half ring stretching, porphyrinReokruang2019-qj
780	<i>S. epi</i>	DNA/RNA ring breathing (cytosine/thymine)[60]	1368	<i>E. coli</i>	$\nu(\text{COO-})$ and $\delta(\text{C-H})$ proteins[60]
799	RBC	$\nu(\text{pyr breathe})$ , $\nu_6$ [57]	1371	RBC	$\nu_4$ [58]
800	<i>S. epi</i>	DNA/RNA ring breathing	1374	RBC	$\nu(\text{pyr half-ring})_{\text{sym}}$ , $\nu_4$ , Proteins, lipids: $\delta(\text{CH}_3)_{\text{sym}}$ [57]
808	<i>E. coli</i>	$\nu(\text{CN})$ Tyr, Val[56]	1386	<i>E. coli</i>	$\delta(\text{CH}_3)$ symmetrical[60]
815	RBC	Ser: $\gamma(\text{COO-})$ [57]	1399	<i>E. coli</i>	C-O-O- stretching in amino acids[60]
823	<i>E. coli</i>	Different C-N stretch[53]	1412	RBC	$\nu(\text{pyr quarter-ring})_{\text{sym}}$ , $\nu_{20}$ , Proteins: COO- sym stretch[57]
826	<i>E. coli</i>	$V_a(\text{O-P-O})$ str.[60]	1421	RBC	$\nu(\text{C}_{\alpha}\text{ph}a\text{C}_m)_{\text{sym}}$
828	RBC	$\gamma(\text{CmH})$ [57]	1422	RBC	$\nu_{28}$ [58]
848	<i>S. epi</i>	Thymine[60]	1440	<i>S. epi</i>	protein or lipid[55]
851	<i>E. coli</i>	Thymine[60]		RBC	CH <sub>2</sub> deformation - lipid, protein[59]
855	RBC	$\gamma$ -Porphyrin[57]	1446	<i>S. epi</i>	Scissoring (fatty acids, phospholipids, and mono- and oligo-saccharides); CH <sub>2</sub> /CH <sub>3</sub> deformation[60]

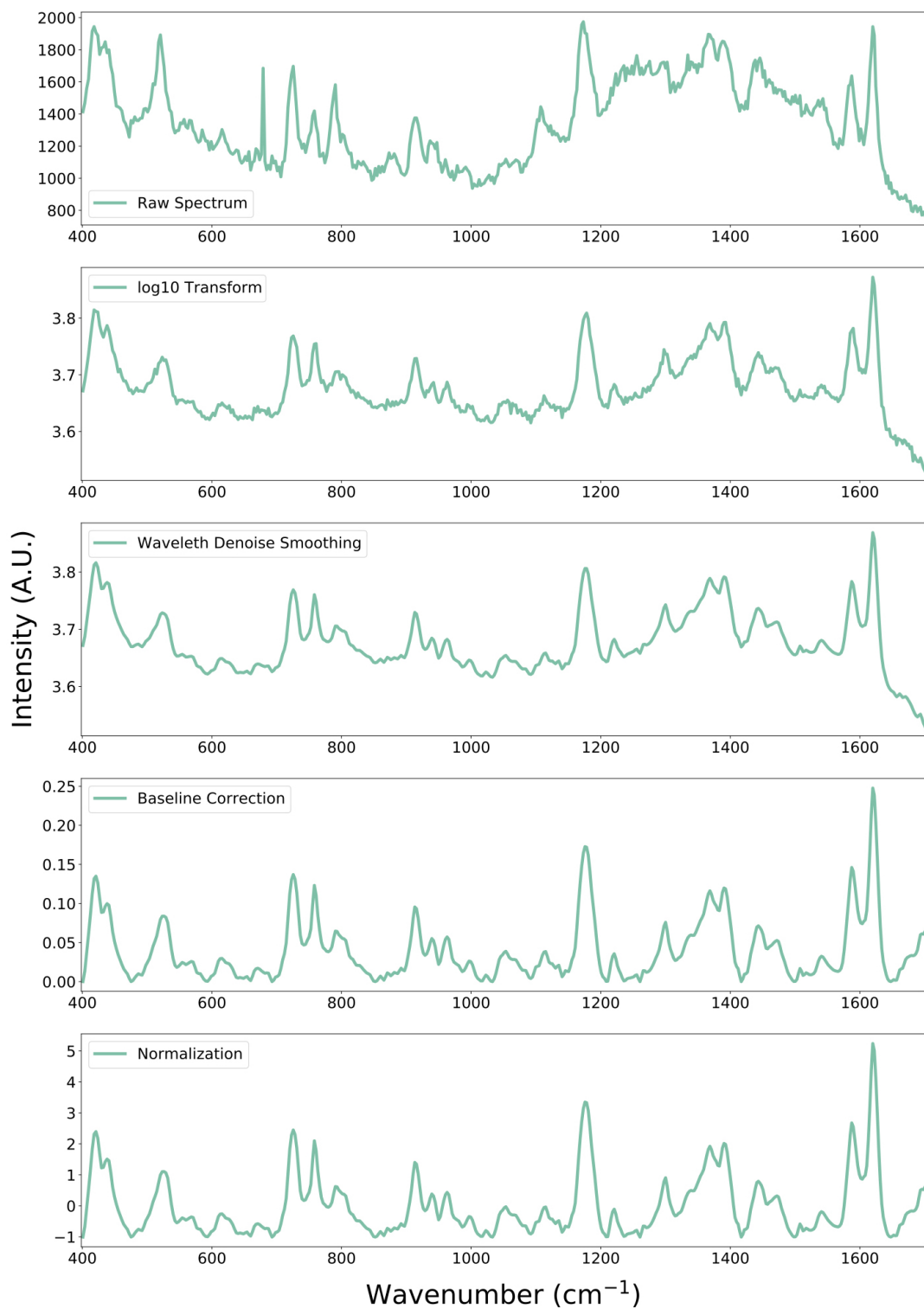
Peak Pos. ( $\text{cm}^{-1}$ )	Cell Type	Peak Assignment	Peak Pos. ( $\text{cm}^{-1}$ )	Cell Type	Peak Assignment
871	RBC	$\gamma(\text{C}_m\text{H})$ [57], $\gamma_{10}$	1449	<i>E. coli</i>	Scissoring (fatty acids, phospholipids, and mono-oligo-saccharides); $\text{CH}_2/\text{CH}_3$ deformation[60]
912	RBC	Glu, Ile, Thr, Lys: C-C stretch[57]	1450	<i>E. coli</i>	$\text{CH}_2/\text{CH}_3$ deformation of proteins and lipids[52]
924	RBC	Amino acids: C-COO-stretch[57]	1452	RBC	$\delta(\text{CH}_2/\text{CH}_3)$ , Lipids: $\delta(\text{CH}_2/\text{CH}_3)$ [57]
944	RBC	$\nu_{46}$ [58]	1465	RBC	$\nu(\text{C}_\alpha\text{C}_m)_{\text{sym}}$ , $\nu_3$ , Lipids: $\delta(\text{CH}_2/\text{CH}_3)$ [57]
950	<i>S. epi</i>	$\nu(\text{CH}_3)$ of proteins (a-helix)[60]	1472	<i>E. coli</i>	$\text{CH}_2$ deformation of the protein molecules[50, 51]
952	RBC	$\gamma(\text{C}_a\text{H} =)$ [57]	1492	RBC	trp:indole ring bend, indole CH bend[57]
955	<i>E. coli</i>	$\nu(\text{CH}_3)$ of proteins (a-helix)[60] $\nu(\text{CN})$ [56] C=C deformation[52]	1495	<i>S. epi</i>	$\delta(\text{CH}_2)$ [60]
960	<i>E. coli</i> [50] RBC	$\delta(\text{C}=\text{C})$ or tyrosine	1511	RBC	$\nu_{38}$ [58]
967	RBC	Proteins: C-C stretch[57]	1529	<i>S. epi</i>	Amide II of proteins, N-acetyl related bands (amide II)[60]
974	<i>E. coli</i>	C=C deformation[53]	1533	<i>E. coli</i>	Amide II of proteins, N-acetyl related bands (amide II)[60]
982	RBC	$\gamma(\text{C}_a\text{H} =)$ [57]	1535	<i>E. coli</i>	adenine, cytosine, and guanine[60]
997	<i>E. coli</i>	Phe or glucose[50]	1538	<i>S. epi</i>	Amide II of proteins[60]

Peak Pos. (cm <sup>-1</sup> )	Cell Type	Peak Assignment	Peak Pos. (cm <sup>-1</sup> )	Cell Type	Peak Assignment
1000	<i>E. coli</i>	Phe[60]	1543	RBC	$\nu_{11}$ [58]
1002	<i>S. epi</i>	Phe[60]	1550	RBC	$\nu(C_\beta C_\beta)$ , $\nu_{11}$ , Proteins, lipids: amide II, Trp[57]
1006	RBC	Phe: indole asymmetric ring breathe[57]	1553	<i>E. coli</i>	Amide II of proteins[60]
1010	RBC	$\nu_{45}$ [58]			
1013	RBC	Trp: indole asymmetric ring breathe[57]	1558	RBC <i>E. coli</i>	N-H, Trp[59] CH <sub>2</sub> deformation[53]
1027	<i>E. coli</i>	A Ring stretching or (C-H) deformation[50]	1564	<i>S. epi</i>	Amide II of proteins, guanine/adenine[60]
1030	<i>E. coli</i> RBC	Phe: C-H in plane bending[60] Phe: in-plane ring CH deform[57]	1575	RBC	skeletal mode, trp[57]
1032	<i>S. epi</i>	Phe: C-H in plane bending[60]	1579	<i>E. coli</i>	Guanine, adenine, trp (proteins)[59]
1040	<i>S. epi</i> RBC	$\nu(CC)$ aromatic ring[60] $\delta(=C_b H_2)_{asym}$ [57]	1582	RBC	C-C asymmetric stretching, hemoglobin[59]
1056	<i>E. coli</i>	Stretching vibration of C-C in alkanes[51]	1590	<i>E. coli</i> RBC	Phe, hydroxyproline, Tyr[52] $\nu(C_\alpha C_m)_{asym}$ , $\nu_{37}$ , Phe, Tyr[57]
1086	<i>E. coli</i>	Phe[50]	1600	<i>S. epi</i>	Protein and carboxylic stretches[55]
1090	<i>E. coli</i>	C-C skeletal and C-O-C stretch- ing from glycosidic link[52] $=C_{2vinyl}H$ [57] $\nu_s(PO_2)$ [60]		<i>E. coli</i>	Protein and carboxylic stretches[55]
1094	RBC		1601	<i>E. coli</i>	Tyr, C-N stretching vibration
1096	<i>S. epi</i>		1609	RBC	$\nu(C_a = C_b)$ , $\nu(C = C)_{vinyl}$ [57]
			1614	<i>E. coli</i>	adenine, guanine (ring stretching)[53]

Peak Pos. ( $\text{cm}^{-1}$ )	Cell Type	Peak Assignment	Peak Pos. ( $\text{cm}^{-1}$ )	Cell Type	Peak Assignment
1097	<i>E. coli</i>	$\nu_s(PO_2)$ [60]	1617	RBC	C=C trp, tyrosine[59]
1099	<i>E. coli</i>	carbohydrates, C-C, C-O, -C-OH[53]	1620	RBC	$\nu(C=C)_{vinyl}$ [58]
1109	RBC	Proteins, lipids: C-N and C-C stretch[57]	1635	RBC	$\nu(C_\alpha C_m)_{asym}$ , $\nu 10$ [57]
1120	RBC	$\nu 5$ [58]			

**Note:** The Raman shift can vary slightly, depending on cell culture media, bacterial strain, and Raman substrate as well as acquisition parameters including excitation wavelength and temperature[57], and as such, the peak assignments are often treated as approximations[51].

**Abbreviations:** pyr, pyrrol; deform, deformation; sym, symmetric; asym, asymmetric; Cys, cysteine; Lys, lysine; Glu, glutamic acid; Ile, isoleucine; Phe, phenylalanine; Met, methionine; His, histidine; Asp, aspartic acid; Asn, asparagine; Gln, glutamine; Ala, alanine; Leu, leucine; Val, valine; Trp, tryptophan; Ser, serine; Thr, threonine; breathe, breathing; sciss, scissoring; stretch, stretching; wag, wagging. Vibrations:  $\nu$ , valence;  $\delta$ , deformation,  $\gamma$ , deformation (out of plane)[57].



**Supplementary Fig. 26** Spectral Preprocessing. Plot showing a sample spectra taken from our dataset of spectra collected from droplets printed with *E. coli* bacteria and GNRs. Plot shows (from top to bottom) the raw spectrum, the spectrum after a  $\log_{10}$  transformation, spectrum after smoothing using a wavelet denoising, spectrum with baseline correction, and finally the normalized spectrum.

## References

- [1] Indrasekara, A. S. D. S. *et al.* Gold nanostar substrates for SERS-based chemical sensing in the femtomolar regime. *Nanoscale* **6** (15), 8891–8899 (2014) .
- [2] Jackson, J. B. & Halas, N. J. Surface-enhanced raman scattering on tunable plasmonic nanoparticle substrates. *Proc. Natl. Acad. Sci. U. S. A.* **101** (52), 17930–17935 (2004) .
- [3] Alonso-González, P. *et al.* Resolving the electromagnetic mechanism of surface-enhanced light scattering at single hot spots. *Nat. Commun.* **3** (1), 1–7 (2012) .
- [4] Langer, J. *et al.* Present and future of Surface-Enhanced raman scattering. *ACS Nano* **14** (1), 28–117 (2020) .
- [5] Félidj, N. *et al.* Optimized surface-enhanced raman scattering on gold nanoparticle arrays. *Appl. Phys. Lett.* **82** (18), 3095–3097 (2003) .
- [6] Lombardi, J. R. & Birke, R. L. The theory of surface-enhanced raman scattering. *J. Chem. Phys.* **136** (14), 144704 (2012) .
- [7] Andreou, C., Kishore, S. A. & Kircher, M. F. Surface-Enhanced raman spectroscopy: A new modality for cancer imaging. *J. Nucl. Med.* **56** (9), 1295–1299 (2015) .
- [8] Pilot, R. *et al.* A review on Surface-Enhanced raman scattering. *Biosensors* **9** (2) (2019) .
- [9] Schatz, G. C., Young, M. A. & Van Duyne, R. P. in *Electromagnetic mechanism of SERS* (eds Kneipp, K., Moskovits, M. & Kneipp, H.) *Surface-Enhanced Raman Scattering: Physics and Applications* 19–45 (Springer Berlin Heidelberg, Berlin, Heidelberg, 2006).
- [10] Latorre, F. *et al.* Spatial resolution of tip-enhanced raman spectroscopy - DFT assessment of the chemical effect. *Nanoscale* **8** (19), 10229–10239 (2016) .
- [11] Bantz, K. C. *et al.* Recent progress in SERS biosensing. *Phys. Chem. Chem. Phys.* **13** (24), 11551–11567 (2011) .
- [12] Orendorff, C. J., Gearheart, L., Jana, N. R. & Murphy, C. J. Aspect ratio dependence on surface enhanced raman scattering using silver and gold nanorod substrates. *Phys. Chem. Chem. Phys.* **8** (1), 165–170 (2006) .
- [13] Dasary, S. S. R., Singh, A. K., Senapati, D., Yu, H. & Ray, P. C. Gold nanoparticle based Label-Free SERS probe for ultrasensitive and selective

- detection of trinitrotoluene. *J. Am. Chem. Soc.* **131** (38), 13806–13812 (2009) .
- [14] Joseph, V. *et al.* SERS enhancement of gold nanospheres of defined size. *J. Raman Spectrosc.* **42** (9), 1736–1742 (2011) .
  - [15] Stoerzinger, K. A., Lin, J. Y. & Odom, T. W. Nanoparticle SERS substrates with 3D raman-active volumes. *Chem. Sci.* **2** (8), 1435–1439 (2011) .
  - [16] Ha, M. *et al.* Multicomponent plasmonic nanoparticles: From heterostructured nanoparticles to colloidal composite nanostructures. *Chem. Rev.* **119** (24), 12208–12278 (2019) .
  - [17] Sharma, B., Frontiera, R. R., Henry, A.-I., Ringe, E. & Van Duyne, R. P. SERS: Materials, applications, and the future. *Mater. Today* **15** (1), 16–25 (2012) .
  - [18] Kunzmann, A. *et al.* Toxicology of engineered nanomaterials: focus on biocompatibility, biodistribution and biodegradation. *Biochim. Biophys. Acta* **1810** (3), 361–373 (2011) .
  - [19] Shukla, R. *et al.* Biocompatibility of gold nanoparticles and their endocytotic fate inside the cellular compartment: a microscopic overview. *Langmuir* **21** (23), 10644–10654 (2005) .
  - [20] Wen, X. *et al.* PRADA: Portable reusable accurate diagnostics with nanostar antennas for multiplexed biomarker screening. *Bioeng. Transl. Med.* **5** (3), e10165 (2020) .
  - [21] Reguera, J., Langer, J., Jiménez de Aberasturi, D. & Liz-Marzán, L. M. Anisotropic metal nanoparticles for surface enhanced raman scattering. *Chem. Soc. Rev.* **46** (13), 3866–3885 (2017) .
  - [22] An’Nisa, N. Z., Morsin, M., Sanudin, R., Razali, N. L. & Nafisah, S. Controlled wet chemical synthesis of gold nanorods for triclopyr butotyl herbicide detection based-plasmonic sensor. *Sensing and Bio-Sensing Research* **29**, 100359 (2020) .
  - [23] Jain, P. K., Lee, K. S., El-Sayed, I. H. & El-Sayed, M. A. Calculated absorption and scattering properties of gold nanoparticles of different size, shape, and composition: applications in biological imaging and biomedicine. *J. Phys. Chem. B* **110** (14), 7238–7248 (2006) .
  - [24] Lin, K.-Q. *et al.* Size effect on SERS of gold nanorods demonstrated via single nanoparticle spectroscopy. *J. Phys. Chem. C* **120** (37), 20806–20813 (2016) .

- [25] Sharma, V., Park, K. & Srinivasarao, M. Colloidal dispersion of gold nanorods: Historical background, optical properties, seed-mediated synthesis, shape separation and self-assembly. *Mater. Sci. Eng. R Rep.* **65** (1), 1–38 (2009) .
- [26] Ye, X., Zheng, C., Chen, J., Gao, Y. & Murray, C. B. Using binary surfactant mixtures to simultaneously improve the dimensional tunability and monodispersity in the seeded growth of gold nanorods. *Nano Lett.* **13** (2), 765–771 (2013) .
- [27] Baumberg, J. J., Aizpurua, J., Mikkelsen, M. H. & Smith, D. R. Extreme nanophotonics from ultrathin metallic gaps. *Nat. Mater.* **18** (7), 668–678 (2019) .
- [28] Yu, Q., Guan, P., Qin, D., Golden, G. & Wallace, P. M. Inverted size-dependence of surface-enhanced raman scattering on gold nanohole and nanodisk arrays. *Nano Lett.* **8** (7), 1923–1928 (2008) .
- [29] Reilly, T. H., Chang, S.-H., Corbman, J. D., Schatz, G. C. & Rowlen, K. L. Quantitative evaluation of plasmon enhanced raman scattering from nanoaperture arrays. *J. Phys. Chem. C* **111** (4), 1689–1694 (2007) .
- [30] Zhang, K. *et al.* Large-Area graphene nanodot array for Plasmon-Enhanced infrared spectroscopy. *Small* **12** (10), 1302–1308 (2016) .
- [31] Kumar, G. V. P. *et al.* Hot spots in ag Core-Au shell nanoparticles potent for Surface-Enhanced raman scattering studies of biomolecules. *J. Phys. Chem. C* **111** (11), 4388–4392 (2007) .
- [32] Yin, Y. D., Gao, L. & Qiu, C. W. Electromagnetic theory of tunable SERS manipulated with spherical anisotropy in coated nanoparticles. *J. Phys. Chem. C* **115** (18), 8893–8899 (2011) .
- [33] Jackson, J. B., Westcott, S. L., Hirsch, L. R., West, J. L. & Halas, N. J. Controlling the surface enhanced raman effect via the nanoshell geometry. *Appl. Phys. Lett.* **82** (2), 257–259 (2003) .
- [34] Hadimioglu, B. *et al.* IEEE (ed.) *Acoustic ink printing*. (ed.IEEE) *IEEE 1992 Ultrasonics Symposium Proceedings*, 929–935 vol.2 (1992).
- [35] Elrod, S. A. *et al.* Nozzleless droplet formation with focused acoustic beams. *J. Appl. Phys.* **65** (9), 3441–3447 (1989) .
- [36] Chu, B. & Apfel, R. E. Acoustic radiation pressure produced by a beam of sound. *J. Acoust. Soc. Am.* **72** (6), 1673–1687 (1982) .

- [37] Rayleigh, J. W. *The Theory of Sound, 2nd Ed.* (Dover Publications, New York, 1945).
- [38] Fang, Y. *et al.* Rapid generation of multiplexed cell cocultures using acoustic droplet ejection followed by aqueous two-phase exclusion patterning. *Tissue Eng. Part C Methods* **18** (9), 647–657 (2012) .
- [39] Hadimioglu, B., Stearns, R. & Ellson, R. Moving liquids with sound: The physics of acoustic droplet ejection for robust laboratory automation in life sciences. *J. Lab. Autom.* **21** (1), 4–18 (2016) .
- [40] Eisenmenger, W. Dynamic properties of the surface tension of water and aqueous solutions of surface active agents with standing capillary waves in the frequency range from 10 kc/s to 1.5 mc/s. *Acta Acustica united with Acustica* **9** (4), 327–340 (1959) .
- [41] Hadimioglu, B., Elrod, S. & Sprague, R. Yuhas, D. & Schneider, S. (eds) *Acoustic ink printing: an application of ultrasonics for photographic quality printing at high speed.* (eds Yuhas, D. & Schneider, S.) *2001 IEEE Ultrasonics Symposium. Proceedings. An International Symposium (Cat. No.01CH37263)*, Vol. 1, 627–635 vol.1 (2001).
- [42] Gu, Q. *et al.* Three-dimensional bio-printing. *Sci. China Life Sci.* **58** (5), 411–419 (2015) .
- [43] Demirci, U. & Montesano, G. Single cell epitaxy by acoustic picolitre droplets. *Lab Chip* **7** (9), 1139–1145 (2007) .
- [44] Roessler, C. G. *et al.* Acoustic injectors for Drop-On-Demand serial femtosecond crystallography. *Structure* **24** (4), 631–640 (2016) .
- [45] Fuller, F. D. *et al.* Drop-on-demand sample delivery for studying biocatalysts in action at x-ray free-electron lasers. *Nat. Methods* **14** (4), 443–449 (2017) .
- [46] Soares, A. S. *et al.* Acoustically mounted microcrystals yield high-resolution x-ray structures. *Biochemistry* **50** (21), 4399–4401 (2011) .
- [47] Rasmussen, L., White, E. L. & Bostwick, J. R. Acoustic droplet ejection applications for High-Throughput screening of infectious agents. *J. Lab. Autom.* **21** (1), 188–197 (2016) .
- [48] Aerni, H.-R., Cornett, D. S. & Caprioli, R. M. Automated acoustic matrix deposition for MALDI sample preparation. *Anal. Chem.* **78** (3), 827–834 (2006) .

- [49] Tadesse, L. F. *et al.* Plasmonic and electrostatic interactions enable uniformly enhanced liquid bacterial Surface-Enhanced raman scattering (SERS). *Nano Lett.* **20** (10), 7655–7661 (2020) .
- [50] Su, L., Zhang, P., Zheng, D.-W., Wang, Y.-J.-Q. & Zhong, R.-G. Rapid detection of escherichia coli and salmonella typhimurium by surface-enhanced raman scattering. *Optoelectronics Letters* **11**, 157–160 (2015) .
- [51] Moghtader, F., Tomak, A., Zareie, H. M. & Piskin, E. Bacterial detection using bacteriophages and gold nanorods by following time-dependent changes in raman spectral signals. *Artif. Cells Nanomed. Biotechnol.* **46** (sup2), 122–130 (2018) .
- [52] Witkowska, E., Niciński, K., Korsak, D., Szymborski, T. & Kamińska, A. Sources of variability in SERS spectra of bacteria: comprehensive analysis of interactions between selected bacteria and plasmonic nanostructures. *Anal. Bioanal. Chem.* **411** (10), 2001–2017 (2019) .
- [53] Wang, Y., Lee, K. & Irudayaraj, J. Silver nanosphere SERS probes for sensitive identification of pathogens. *J. Phys. Chem. C* **114** (39), 16122–16128 (2010) .
- [54] Sivanesan, A. *et al.* Nanostructured silver–gold bimetallic SERS substrates for selective identification of bacteria in human blood. *Analyst* **139** (5), 1037–1043 (2014) .
- [55] Choi, J., Lee, J. & Jung, J. H. Fully integrated optofluidic SERS platform for real-time and continuous characterization of airborne microorganisms **169**, 112611 (2020) .
- [56] Zhou, H. *et al.* SERS detection of bacteria in water by in situ coating with ag nanoparticles. *Anal. Chem.* **86** (3), 1525–1533 (2014) .
- [57] Drescher, D., Büchner, T., McNaughton, D. & Kneipp, J. SERS reveals the specific interaction of silver and gold nanoparticles with hemoglobin and red blood cell components. *Phys. Chem. Chem. Phys.* **15** (15), 5364–5373 (2013) .
- [58] Premasiri, W. R., Lee, J. C. & Ziegler, L. D. Surface-enhanced raman scattering of whole human blood, blood plasma, and red blood cells: cellular processes and bioanalytical sensing. *J. Phys. Chem. B* **116** (31), 9376–9386 (2012) .
- [59] Reokrungruang, P., Chatnuntawe, I., Dharakul, T. & Bamrungsap, S. A simple paper-based surface enhanced raman scattering (SERS) platform and magnetic separation for cancer screening. *Sens. Actuators B Chem.*

**285**, 462–469 (2019) .

- [60] Paccotti, N. *et al.* Label-Free SERS discrimination and in situ analysis of life cycle in escherichia coli and staphylococcus epidermidis. *Biosensors* **8** (4) (2018) .